Electrical coherent driving of chiral antiferromagnet

Yutaro Takeuchi[1,2,3]*, Yuma Sato[4,5], Yuta Yamane[4,6]*, Ju-Young Yoon[4,5], Yukinori Kanno[4,5], Tomohiro Uchimura[4,5], K. Vihanga De Zoysa[4,5], Jiahao Han[1,4], Shun Kanai[1,4,5,7,8,9], Jun'ichi Ieda[10], Hideo Ohno[1,4,7,11], and Shunsuke Fukami[1,4,5,7,11,12]*

Affiliations:

[1]Advanced Institute for Materials Research, Tohoku University; Sendai, 980-8577, Japan.
[2]International Center for Young Scientists, National Institute for Materials Science; Tsukuba, 305-0047, Japan.
[3]Research Center for Magnetic and Spintronics Materials, National Institute for Materials Science; Tsukuba, 305-0047, Japan.
[4]Laboratory for Nanoelectronics and Spintronics, Research Institute for Electrical Communication, Tohoku University; Sendai, 980-8577, Japan.
[5]Graduate School of Engineering, Tohoku University; Sendai, 980-0845, Japan.
[6]Frontier Research Institute for Interdisciplinary Sciences, Tohoku University; Sendai, 980-8578, Japan
[7]Center for Science and Innovation in Spintronics, Tohoku University; Sendai, 980-8577, Japan
[8]Division for the Establishment of Frontier Sciences of Organization for Advanced Studies at Tohoku University; Sendai, 980-8577, Japan
[9]National Institutes for Quantum Science and Technology; Takasaki, 370-1292, Japan
[10]Advanced Science Research Center, Japan Atomic Energy Agency; Tokai, Ibaraki, 319-1195, Japan
[11]Center for Innovative Integrated Electronic Systems, Tohoku University; Sendai, 980-0845, Japan
[12]Inamori Research Institute for Science; Kyoto, 600-8411, Japan
* Corresponding author. Email: takeuchi.yutaro@nims.go.jp, yutaymn@tohoku.ac.jp, s-fukami@tohoku.ac.jp

Abstract: Electric current driving of antiferromagnetic states at radio or higher frequencies remains challenging to achieve. Here we report all-electrical, gigahertz-range, coherent driving of chiral antiferromagnet Mn_3Sn nanodot samples. High coherence in multiple trials and threshold current insensitive to pulse width, in contrast to ferromagnets, are achieved in sub-nanosecond range, allowing 1,000/1,000 switching by 0.1-ns pulses at zero field. These features are attributed to the inertial nature of antiferromagnetic excitations. Our study highlights the potential of antiferromagnetic spintronics to combine high speed and high efficiency in magnetic device operations.

Electrical manipulation of collective spin states is a central subject of magnetics and spintronics, and various physical schemes have been demonstrated mostly with ferromagnetic systems (*1*–*3*). The spin-orbit torque (SOT) (*4*–*6*), a relativistic phenomenon originating from the spin Hall effect (*7*) and/or Rashba-Edelstein effect (*8*) in magnetic heterostructures, has been recently applied to antiferromagnets (*9*–*11*). One of the prospective advantages of antiferromagnets over ferromagnets is their potential for faster driving with higher efficiency owing to the exchange-enhanced intrinsic frequency (*12*) and the inertia in their dynamics (*13*). Ultrafast switching of ferromagnets has been recently reported; however, it required relatively large current densities and the assistance of external fields and thermal effects (*14*, *15*). For antiferromagnets, an electrical control was achieved by the staggered SOT (*16*), which emerges in locally noncentrosymmetric crystals (*16*–*20*). Later, the standard SOT in antiferromagnet/nonmagnet heterostructures was demonstrated to be capable of switching (*21*–*27*) and continuously rotating (*28*, *29*) antiferromagnetic spin states. In pursuit of revealing the high-speed dynamics of antiferromagnets, earlier works reported switching of antiferromagnets by picosecond laser pulses (*30*, *31*) and an efficient excitation and ultrafast propagation of antiferromagnetic magnons (*32*–*34*). However, all-electrical switching of an antiferromagnet, required for electronic devices, has been limited in timescales longer than nanoseconds, where the results can be understood by an extrapolation from the DC-regime experiments. Despite the promising prospect for all-electrical switching of antiferromagnets with a combination of high speed and high efficiency that cannot be reached with ferromagnets, its experimental exploration remains challenging.

Here we show all-electrical driving of a chiral antiferromagnetic Mn_3Sn nanodot by single electric pulses in GHz range, through coherent spin excitations in a single antiferromagnetic

domain. In contrast to ferromagnets, where fast electrical control at the timescale of 0.1 ns and beyond is challenging because of significant increase in the threshold current (*35–39*), we show that it is not the case for antiferromagnets. The markedly suppressed increase in the driving current in sub-nanosecond range, combined with a high coherence of the employed system, allows us to achieve 1,000/1,000 switching by 0.1-ns pulses at zero magnetic field. The observed advantage of antiferromagnets over ferromagnets can be attributed to the universal inertial nature of antiferromagnetic dynamics, as indicated by our theoretical modeling.

Sample structure and measurement layout for control of coherent rotation in chiral antiferromagnet Mn_3Sn nanodot

To realize a coherent control of the antiferromagnetic order, we fabricate Mn_3Sn / heavy metal heterostructure-based nanodot samples. The stack structure consists of W(2 nm) / Ta(3 nm) / Mn_3Sn(20 nm) / MgO(1.3 nm) / Ru(1 nm), which is deposited on MgO(110) substrate by sputtering [Materials and Methods (*40*)]. We confirm $(1\bar{1}00)$-plane (M-plane) oriented, epitaxial Mn_3Sn films where the kagome plane is perpendicular to the film plane (Fig. S1) (*28*, *41*). The films are processed into Hall-bar devices, where a Mn_3Sn nanodot is formed on a cross-shaped W/Ta channel (Fig. 1A) (*40*). The nominal dot diameter *D*, channel width, and channel length are 200 nm, 250 nm, and 600 nm, respectively. An image of a fabricated nanodot sample taken by scanning electron microscopy is displayed in Fig. 1B. After defining the Hall-cross with a nanodot, coplanar waveguides are formed for high-frequency measurements.

Our experimental setup for electrical driving of Mn_3Sn is shown in Fig. 1C. We apply a pulse voltage with the width of 0.1-10 ns using a pulse generator through an RF port of the bias tee. The state of the chiral spin structure in Mn_3Sn is detected through the anomalous Hall effect (*42*) by measuring the voltage between the two Hall probes under a DC current of 100 μA, corresponding to the current density in W/Ta layer of 3.8 MA cm^{-2}, applied to the DC port of the bias tee. The

output side of the waveguide is terminated by an oscilloscope with an impedance of 50 Ω, which is used to monitor the transmitted waveforms of the injected pulses. Shown in Fig. 1D is the captured transmitted waveform of the applied pulse with nominal width of 0.1 ns (details on the captured waveforms with various nominal pulse widths are summarized in Fig. S2). Notice that the pulse voltage is applied in the $[11\bar{2}0]$ direction of the hexagonal Mn_3Sn film, which is the most effective configuration for the Slonczewski-like SOT to induce the chiral-spin rotation (*28*, *29*).

Figure 2A shows the Hall resistance R_H vs. the out-of-plane magnetic field H_z in a Mn_3Sn nanodot with D = 200 nm, where D is the nanodot diameter. Negative anomalous Hall resistance and binary state in the hysteresis loop are observed, consistent with our previous study on the thermal stability of Mn_3Sn nanodots (*43*), where the uniaxial perpendicular anisotropy and the exchange stiffness for the antiferromagnetic order have been determined as 370 Jm^{-3} and 3.5 pJm^{-1}, respectively, leading to the domain wall width of ~ 300 nm. The switching field in the present study is evaluated to be about 350 mT (Fig. 2A).

Hall resistance vs. applied current in Mn_3Sn nanodot

Before performing all-electrical experiments in GHz range, we establish the field-free continuous rotation and field-assisted bipolar switching of the Mn_3Sn nanodots in DC regime. Figure 2B shows R_H vs. J_{HM} in a Mn_3Sn nanodot with D = 200 nm, where J_{HM} denotes the current density flowing into the W/Ta heavy metal layers [Sections S3 and S4 of (*40*)]. The field H_x is also applied to the $[11\bar{2}0]$ direction of Mn_3Sn, *i.e.*, parallel to the current. For $\mu_0 H_x$ = 0 mT, the binary randomization of R_H is observed above the threshold current density, regardless of the pulse current direction. This is attributed to the SOT-driven continuous rotation of the chiral antiferromagnetic order in Mn_3Sn (*28*, *44*). The randomization between the binary states shows that the predominant magnetic anisotropy is twofold with the easy axis normal

to the film (*24*, *29*) and that the Mn_3Sn nanodot has a single-domain structure (*43*). With finite H_x, a bipolar switching of R_H is obtained, where the polarity of the hysteresis curve depends on the sign of H_x. This characteristic of the field-assisted switching is consistent with that reported in the previous studies on Hall bar devices (*23–26*, *29*, *44*) and can be explained as a result of the SOT-driven rotation being balanced by the external field that prefers the uncompensated net magnetization of Mn_3Sn pointing parallel to H_x.

We then move onto experiments with short current pulses in the range of ns ~ sub-ns. We first check the field-assisted switching by the short current pulses. Shown in Fig. 2C are R_H-J_{HM} curves with the pulse width τ = 0.1 ns and $\mu_0 H_x = \pm 300$ mT; the R_H-J_{HM} curves at $\mu_0 H_x$ = 300 mT with various τ are displayed in Fig. 2D. J_{HM} is calculated from the peak amplitude of the transmitted waveform. Bipolar switching is observed for all the τ down to 0.1 ns at $J_{HM} < 75$ MAcm^{-2}. In the following sections, the relationship between the pulse width and the threshold current density is extensively investigated.

Switching probability vs. pulse width and amplitude

For deeper investigation into the dynamics of the chiral-spin structure in Mn_3Sn nanodots in the GHz regime, we measure the switching probability P as a function of J_{HM}, τ, and H_x by multiple applications of current pulses [see Section S5 of (*40*) and Fig. S5 for more details]. Here, P is defined as the ratio of the number of successful switching out of at least 50 attempts of pulse application for a given set of J_{HM}, τ, and H_x. The antiferromagnetic ordering is initialized by applying 0.1-s pulse current with an amplitude of 42 MAcm^{-2} under $\mu_0 H_x$ = 300 mT.

Figures 3, A-D, show the P vs. J_{HM} for τ = 0.1, 0.2, 0.3, and 1.0 ns, respectively, under $\mu_0 H_x$ = 0 and 300 mT. A general tendency for the case with $\mu_0 H_x$ = 300 mT is that P initially increases with J_{HM}, reaches 1 and starts decreasing as J_{HM} further increases. The range of J_{HM} achieving P = 1 expands with a reduction of τ. This observation indicates that the antiferromagnetic order

acquires a lower probability to switch back to the original state with the shorter pulse widths. Under a longer and larger pulse, the chiral antiferromagnetic order experiences a larger driving force to rotate for a longer time, resulting in less predictability for the final state. For $\mu_0 H_x = 0$ mT, non-deterministic behavior ($P \sim 0.5$) above a threshold is observed at $\tau = 1.0$ ns as expected from Fig. 2B; interestingly, there is a $P = 1$ range at $\tau = 0.1$ and 0.2 ns, achieving all-electrical switching, which at this timescale has been seen only in current-induced heat driven reversal of GdFeCo (*45*).

The dependencies of P on τ, J_{HM}, and H_x are summarized by two-dimensional color maps in Fig. 3, E-H. In the regions where J_{HM} is sufficiently large (the upper regions of the color maps), P oscillates with τ between relatively high values (switched regions) and relatively low values (switched-back regions). At $\mu_0 H_x = 0$ mT (Fig. 3E), we confirm a periodic appearance of switched and switched-back regions at least seven times as labeled by the arrows, indicating a highly coherent rotation of chiral-spin structure in the 50 trials. The oscillation of P becomes less appreciable as τ increases. The switched and switched-back regions are shifted toward the right side (longer τ) with decreasing J_{HM}. As $\mu_0 H_x$ increases from 0 to 300 mT, the switched (switched-back) regions expand (shrink). This is because the in-plane magnetic field breaks the $\pm x$ symmetry, assisting the "up" to "down" spin rotation (switching) and hindering the "down" to "up" rotation (switching-back).

The switching and switching-back processes through the coherent chiral spin rotation are schematically illustrated in Fig. 3 I and J. It is theoretically predicted that the frequency of the SOT-driven chiral spin rotation increases with J_{HM} (*28*). Exploiting this unconventional current dependence of the antiferromagnetic dynamics, the switching and switching-back of the antiferromagnetic order can be all electrically controlled by current pulses with $\tau \sim (2N–1)\ \tau_{180}$ and $2N\tau_{180}$, respectively, where N is a positive integer and τ_{180} is the time period for 180° rotation under the given J_{HM}. In Fig. 3, E-H, the first, second, …, N-th switched (switched-back) regions therefore

correspond to the coherent chiral spin rotation being completed one, three, …, 2*N-1* (two, four, …, 2*N*) times. This is consistent with our numerical calculation considering the SOT-driven chiral-spin rotation in a single-domain antiferromagnet without any thermal assistance (Fig. S6). The calculation also shows that the switching characteristic is insensitive to the rise and fall times of the pulse (Fig. S7), indicating a minor impact of the thermally-assisted SOT (*25*, *26*) in our experiment. Notably, although the experimentally observed switching characteristic may appear to be similar to the ferromagnetic switching by a short electric-field pulse (*46*, *47*), our scheme for the antiferromagnetic system does not require an external magnetic field.

Next we demonstrate the reproducibility of the field-free switching based on the coherent driving of the chiral-spin structure. We repeat the write-and-read cycle 1,000 times at zero field, where a writing current pulse of τ = 0.1 ns and J_{HM} = 112 MA cm^{-2} is utilized. Figure 3K shows a portion of the data, with R_H varying with the pulse number; the full results are shown in Fig. S8. It clearly manifests the full switching of the antiferromagnetic state taking place at each pulse application. We observe no error in the 1,000 attempts thanks to the high coherence of the chiral-spin dynamics.

Switching current density vs. pulse width

We now study the switching in more detail, and start by examining the dependence of the switching current density J_C on the pulse width τ. Here, J_C (τ) is defined as the value of J_{HM} at which P first reaches 0.5 at fixed τ. Figure 4A shows the measured τ dependence of J_C for each H_x. The presence of H_x diminishes J_C because in the current configuration H_x assists the switching, as discussed in the previous section. We find that reducing τ from 1 to 0.2 ns (0.1 ns) leads to an increase in J_C by a factor of about 1.2 (1.4). This increasing rate is markedly lower than for ferromagnetic switching. For example, in a three-terminal magnetic tunnel junction comprising of Ta/W/CoFeB/MgO designed to be switched by both spin-orbit and spin-transfer torques, the

reduction of τ from 1 to 0.2 ns was reported to result in an increase in J_C by a factor of about 2.6 (*39*). A similar significant increase in J_C was also reported in a perpendicularly magnetized Pt/Co/AlO_x nanodot (*36*), multilevel magnetization switching in exchange-biased Pt/Co/Ir-Mn (*48*), field-free SOT switching in a CoFeB/Ti/CoFeB nanodot (*49*), and SOT-driven domain wall motion in ferrimagnetic Co-Gd (*50*). In the case of ferromagnetic switching by the conventional spin-transfer torque or the so-called Type-Y SOT switching (*5*, *6*), the rate of J_C increase is even higher (*35*, *37*–*39*). A thorough comparison of the pulse width dependence of the switching current density reported in previous studies on ferromagnets and this work is shown in Fig. S9, showcasing a qualitative difference between the ferromagnets and chiral antiferromagnets. The physical mechanism behind the greater suppression of J_C in Mn_3Sn can be mainly attributed to the inertial nature of the chiral spin rotation, a universal property of antiferromagnetic dynamics. This is discussed in more detail later in theoretical considerations.

Rotation frequency vs. current density

In this section, we evaluate the frequency f_{rot} of the chiral spin rotation in the Mn_3Sn nanodots with respect to the applied current. For this purpose, we extract the P vs. τ at $\mu_0 H_x$ = 0 mT for various J_{HM} shown in Fig. 3E. In Fig. 4B, we show P vs. τ at J_{HM} = 104 MA cm^{-2} as an example, where seven peaks are identified in the oscillation of P. We evaluate f_{rot} from the τ interval between the first and last peaks. Results of the P vs. τ evaluated in the same fashion for various J_{HM} are summarized in Fig. S10. We note that, because of the inertial nature in antiferromagnetic dynamics that will be discussed later, f_{rot} may not be a quantitatively very accurate indicator of the actual frequency of the chiral spin rotation. However, the J_{HM} dependence of f_{rot} (Fig. 4C) displays an important physical feature: f_{rot} increases with J_{HM}, consistent with the theoretical prediction (*28*, *51*). This tunability of the frequency with the current could lead to a different type of electrically tunable spintronic oscillators, in contrast to the conventional ones, where ferromagnetic resonance

is the basic working principle and thus the frequency of the spin dynamics is intrinsic to the system determined by material parameters such as the magnetic anisotropy (*11*, *46*, *52*, *53*).

Theoretical Considerations

Now we theoretically show that the threshold current density with a given pulse width is almost universally lower in antiferromagnets than in ferromagnets in sub-ns regime, because of the inertial nature of the former's equation of motion. The magnetization of a ferromagnet obeys the Landau-Lifshitz-Gilbert (LLG) equation, a first-order differential equation in time. In contrast, the dynamics of the angular variable θ of the antiferromagnetic order parameter in the kagome plane is described by a second-order differential equation in time (*54*, *55*), $(\gamma H_{\mathrm{E}})^{-1}\partial_t^2\theta = -\alpha\partial_t\theta - \frac{\gamma H_K}{2}\sin 2\theta - \gamma H_{\mathrm{S}}$; the left-hand-side is the inertial term with γ the gyromagnetic ratio and H_{E} the effective field associated with the antiferromagnetic exchange coupling. The three "forces" on the right-hand-side originate from, respectively, the damping torque on each sublattice magnetic moment with α the Gilbert damping constant, the uniaxial anisotropy characterized by the effective field H_K, and the SOT with H_{S} the Slonczewski-like effective field. The antiferromagnetic dynamics are therefore mathematically described as a point mass moving in potential hills arising due to the magnetic anisotropy. For successful antiferromagnetic switching, the point mass needs to be supplied with sufficient kinetic energy by the SOT to overcome the potential barrier, and the pulse width can be shorter than the time it takes for the point mass to pass through a peak of the potential (*30*, *31*). In our present experiment, the observed antiferromagnetic advantage over ferromagnets can be attributed to the role that the α term plays in the antiferromagnet, i.e., a frictional force that resists the dynamics of θ. Smaller α, therefore, can generally lead to faster and more energy-efficient driving of θ, hence to smaller $J_{\mathrm{C}}(\tau)$. This is in

stark contrast to the ferromagnetic SOT-switching with the injected spin orthogonal to the magnetization *(3,6)*, where $J_C(\tau)$ depends little on α (*56*).

In Fig. 5, the α dependence of $J_C(\tau)$ obtained by numerical simulations are shown for three different τ, where we computed the dynamics of the magnetization (sublattice magnetic moments) for a ferromagnet (antiferromagnet). The details of the calculations are given in Sections S6 and S11-14 of (*40*). For the antiferromagnet, the parameter values are chosen to reproduce our experimental results with Mn_3Sn. To give a fair comparison between the two systems, for the ferromagnet we employed parameter values that give the same effective magnetic anisotropy energy and Slonczewski-like SOT as for Mn_3Sn. For the unrealistically large $\alpha = 1$, $J_C(\tau)$ takes similar values for the antiferromagnet and ferromagnet. As α decreases, $J_C(\tau)$ for the antiferromagnet is linearly reduced until it hits the minimum value to overcome the energy barrier ($\sim$64 MAcm^{-2}), whereas for the ferromagnet it exhibits little dependence on α. As $\alpha \ll 1$ for most magnetic materials of interest, $J_C(\tau)$ is significantly and almost universally smaller for antiferromagnets. The experimental $J_C(\tau)$ is reproduced quantitatively by the simulation with $\alpha = 0.002$ (Fig. S11). Because the discussion here is based on the fundamental inertial nature of antiferromagnetic dynamics, it holds true with any driving forces including spin-transfer torque (*1*, *35*, *39*) and electric field-induced driving (*46*, *47*). Furthermore, it was found that $J_C(\tau)$ monotonically increases with H_K (Fig. S12). We also find that $J_C(\tau)$ for the antiferromagnet is insensitive to H_E (Fig. S13), confirming that the exchange-enhanced effect has a minor impact here. Dependencies of $J_C(\tau)$ on some other micromagnetic parameters are also shown in Fig. S13, demonstrating that our conclusions are quantitatively robust against changes in those parameters. Simulated antiferromagnetic dynamics in time domain with several different pulses are given in Fig. S14.

Discussion and Outlook

In this work, we show a GHz-range electrical coherent driving of a chiral antiferromagnet under the spin-orbit torque using Mn_3Sn nanodots. The results were consistently described by coherent dynamics of the chiral-spin structure with an electrically tunable rotation frequency. Using this scheme, we demonstrate a highly reproducible, field-free GHz switching of the chiral antiferromagnet. We also show that the driving current for the antiferromagnet is much less sensitive to the pulse width in the high-speed regime, owing to the inertial spin dynamics that is universal to antiferromagnets in general. Furthermore, the switching field of Mn_3Sn nanodot, 350 mT in this work, is one to two orders of magnitude larger than the ferromagnetic counterparts (*5*, *6*, *39*, *57*) owing to the vanishingly small magnetization in Mn_3Sn and the correspondingly small Zeeman energy splitting, offering high robustness against external field. Our results experimentally show the advantage of antiferromagnetic spintronics over the conventional ferromagnetic counterpart.

References and Notes

1. E. B. Myers, D. C. Ralph, J. A. Katine, R. N. Louie, R. A. Buhrman, Current-Induced Switching of Domains in Magnetic Multilayer Devices. *Science* **285**, 867–870 (1999). doi:10.1126/science.285.5429.867

2. H. Ohno, D. Chiba, F. Matsukura, T. Omiya, E. Abe, T. Dietl, Y. Ohno, K. Ohtani, Electric-field control of ferromagnetism. *Nature* **408**, 944–946 (2000). doi:10.1038/35050040

3. I. M. Miron, K. Garello, G. Gaudin, P.-J. Zermatten, M. V. Costache, S. Auffret, S. Bandiera, B. Rodmacq, A. Schuhl, P. Gambardella, Perpendicular switching of a single ferromagnetic layer induced by in-plane current injection. *Nature* **476**, 189–193 (2011). doi:10.1038/nature10309

4. A. Manchon, S. Zhang, Theory of nonequilibrium intrinsic spin torque in a single nanomagnet. *Phys. Rev. B* **78**, 212405 (2008). doi:10.1103/PhysRevB.78.212405

5. L. Liu, C.-F. Pai, Y. Li, H. W. Tseng, D. C. Ralph, R. A. Buhrman, Spin-Torque Switching with the Giant Spin Hall Effect of Tantalum. *Science* **336**, 555–558 (2012). doi:10.1126/science.1218197

6. S. Fukami, T. Anekawa, C. Zhang, H. Ohno, A spin–orbit torque switching scheme with collinear magnetic easy axis and current configuration. *Nat. Nanotech.* **11**, 621–625 (2016). doi:10.1038/nnano.2016.29

7. J. E. Hirsch, Spin Hall Effect. *Phys. Rev. Lett.* **83**, 1834–1837 (1999). doi:10.1103/PhysRevLett.83.1834

8. V. M. Edelstein, Spin polarization of conduction electrons induced by electric current in two-dimensional asymmetric electron systems. *Solid State Communications* **73**, 233–235 (1990). doi:10.1016/0038-1098(90)90963-C

9. T. Jungwirth, X. Marti, P. Wadley, J. Wunderlich, Antiferromagnetic spintronics. *Nat. Nanotech.* **11**, 231–241 (2016). doi:10.1038/nnano.2016.18

10. V. Baltz, A. Manchon, M. Tsoi, T. Moriyama, T. Ono, Y. Tserkovnyak, Antiferromagnetic spintronics. *Rev. Mod. Phys.* **90**, 015005 (2018). doi:10.1103/RevModPhys.90.015005

11. J. Han, R. Cheng, L. Liu, H. Ohno, S. Fukami, Coherent antiferromagnetic spintronics. *Nat. Mater.* **22**, 684–695 (2023). doi:10.1038/s41563-023-01492-6

12. C. Kittel, On the Theory of Ferromagnetic Resonance Absorption. *Phys. Rev.* **73**, 155–161 (1948). doi:10.1103/PhysRev.73.155

13. A. F. Andreev, V. I. Marchenko, Symmetry and the macroscopic dynamics of magnetic materials. *Sov. Phys. Usp.* **23**, 21 (1980). doi:10.1070/PU1980v023n01ABEH004859

14. K. Jhuria, J. Hohlfeld, A. Pattabi, E. Martin, A. Y. Arriola Córdova, X. Shi, R. Lo Conte, S. Petit-Watelot, J. C. Rojas-Sanchez, G. Malinowski, S. Mangin, A. Lemaître, M. Hehn, J. Bokor, R. B. Wilson, J. Gorchon, Spin–orbit torque switching of a ferromagnet with picosecond electrical pulses. *Nat. Electron.* **3**, 680–686 (2020). doi:10.1038/s41928-020-00488-3

15. D. Polley, A. Pattabi, A. Rastogi, K. Jhuria, E. Diaz, H. Singh, A. Lemaitre, M. Hehn, J. Gorchon, J. Bokor, Picosecond spin-orbit torque–induced coherent magnetization switching in a ferromagnet. *Sci. Adv.* **9**, eadh5562 (2023). doi:10.1126/sciadv.adh5562

16. P. Wadley, B. Howells, J. Železný, C. Andrews, V. Hills, R. P. Campion, V. Novák, K. Olejník, F. Maccherozzi, S. S. Dhesi, S. Y. Martin, T. Wagner, J. Wunderlich, F. Freimuth, Y. Mokrousov, J. Kuneš, J. S. Chauhan, M. J. Grzybowski, A. W. Rushforth, K. W. Edmonds, B. L. Gallagher, T. Jungwirth, Electrical switching of an antiferromagnet. *Science* **351**, 587–590 (2016). doi:10.1126/science.aab103

17. J. Železný, H. Gao, K. Výborný, J. Zemen, J. Mašek, A. Manchon, J. Wunderlich, J. Sinova, T. Jungwirth, Relativistic Néel-Order Fields Induced by Electrical Current in Antiferromagnets. *Phys. Rev. Lett.* **113**, 157201 (2014). doi:10.1103/PhysRevLett.113.157201

18. S. Y. Bodnar, L. Šmejkal, I. Turek, T. Jungwirth, O. Gomonay, J. Sinova, A. A. Sapozhnik, H.-J. Elmers, M. Kläui, M. Jourdan, Writing and reading antiferromagnetic Mn_2Au by Néel spin-orbit torques and large anisotropic magnetoresistance. *Nat. Commun.* **9**, 348 (2018). doi:10.1038/s41467-017-02780-x

19. M. Meinert, D. Graulich, T. Matalla-Wagner, Electrical Switching of Antiferromagnetic Mn_2Au and the Role of Thermal Activation. *Phys. Rev. Applied* **9**, 064040 (2018). doi:10.1038/s41467-017-02780-x

20. K. A. Omari, L. X. Barton, O. Amin, R. P. Campion, A. W. Rushforth, A. J. Kent, P. Wadley, K. W. Edmonds, Low-energy switching of antiferromagnetic CuMnAs/GaP using sub-10 nanosecond current pulses. *J. Appl. Phys.* **127**, 193906 (2020). /doi.org/10.1063/5.0006183

21. X. Z. Chen, R. Zarzuela, J. Zhang, C. Song, X. F. Zhou, G. Y. Shi, F. Li, H. A. Zhou, W. J. Jiang, F. Pan, Y. Tserkovnyak, Antidamping-Torque-Induced Switching in Biaxial Antiferromagnetic Insulators. *Phys. Rev. Lett.* **120**, 207204 (2018). doi:10.1103/PhysRevLett.120.207204

22. T. Moriyama, K. Oda, T. Ohkochi, M. Kimata, T. Ono, Spin torque control of antiferromagnetic moments in NiO. *Sci. Rep.* **8**, 14167 (2018). doi:10.1038/s41598-018-32508-w

23. H. Tsai, T. Higo, K. Kondou, T. Nomoto, A. Sakai, A. Kobayashi, T. Nakano, K. Yakushiji, R. Arita, S. Miwa, Y. Otani, S. Nakatsuji, Electrical manipulation of a topological antiferromagnetic state. *Nature* **580**, 608–613 (2020). doi:10.1038/s41586-020-2211-2

24. T. Higo, K. Kondou, T. Nomoto, M. Shiga, S. Sakamoto, X. Chen, D. Nishio-Hamane, R. Arita, Y. Otani, S. Miwa, S. Nakatsuji, Perpendicular full switching of chiral antiferromagnetic order by current. *Nature* **607**, 474–479 (2022). doi:10.1038/s41586-022-04864-1

25. B. Pal, B. K. Hazra, B. Göbel, J.-C. Jeon, A. K. Pandeya, A. Chakraborty, O. Busch, A. K. Srivastava, H. Deniz, J. M. Taylor, H. Meyerheim, I. Mertig, S.-H. Yang, S. S. P. Parkin, Setting of the magnetic structure of chiral kagome antiferromagnets by a seeded spin-orbit torque. *Sci. Adv.* **8**, eabo5930 (2022). doi:10.1126/sciadv.abo5930

26. G. K. Krishnaswamy, G. Sala, B. Jacot, C.-H. Lambert, R. Schlitz, M. D. Rossell, P. Nöel, P. Gambardella, Time-Dependent Multistate Switching of Topological Antiferromagnetic Order in Mn_3Sn. *Phys. Rev. Applied* **18**, 024064 (2022). doi:10.1103/PhysRevApplied.18.024064

27. P. Zhang, C.-T. Chou, H. Yun, B. C. McGoldrick, J. T. Hou, K. A. Mkhoyan, L. Liu, Control of Néel Vector with Spin-Orbit Torques in an Antiferromagnetic Insulator with Tilted Easy Plane. *Phys. Rev. Lett.* **129**, 017203 (2022). doi:10.1103/PhysRevLett.129.017203

28. Y. Takeuchi, Y. Yamane, J.-Y. Yoon, R. Itoh, B. Jinnai, S. Kanai, J. Ieda, S. Fukami, H. Ohno, Chiral-spin rotation of non-collinear antiferromagnet by spin–orbit torque. *Nat. Mater.* **20**, 1364–1370 (2021). doi:10.1038/s41563-021-01005-3

29. J.-Y. Yoon, P. Zhang, C.-T. Chou, Y. Takeuchi, T. Uchimura, J. T. Hou, J. Han, S. Kanai, H. Ohno, S. Fukami, L. Liu, Handedness anomaly in a non-collinear antiferromagnet under spin–orbit torque. *Nat. Mater.* **22**, 1106–1113 (2023). doi:10.1038/s41563-023-01620-2

30. A. V. Kimel, B. A. Ivanov, R. V. Pisarev, P. A. Usachev, A. Kirilyuk, T. Rasing, Inertia-driven spin switching in antiferromagnets. *Nat. Phys.* **5**, 727–731 (2009). doi:10.1038/nphys1369

31. K. Olejník, T. Seifert, Z. Kašpar, V. Novák, P. Wadley, R. P. Campion, M. Baumgartner, P. Gambardella, P. Němec, J. Wunderlich, J. Sinova, P. Kužel, M. Müller, T. Kampfrath, T. Jungwirth, Terahertz electrical writing speed in an antiferromagnetic memory. *Sci. Adv.* **4**, eaar3566 (2018). doi:10.1126/sciadv.aar3566

32. Y. Wang, D. Zhu, Y. Yang, K. Lee, R. Mishra, G. Go, S.-H. Oh, D.-H. Kim, K. Cai, E. Liu, S. D. Pollard, S. Shi, J. Lee, K. L. Teo, Y. Wu, K.-J. Lee, H. Yang, Magnetization switching by magnon-mediated spin torque through an antiferromagnetic insulator. *Science* **366**, 1125–1128 (2019). doi: 10.1126/science.aav8076

33. K. Lee, D.-K. Lee, D. Yang, R. Mishra, D.-J. Kim, S. Liu, Q. Xiong, S. K. Kim, K.-J. Lee, H. Yang, Superluminal-like magnon propagation in antiferromagnetic NiO at nanoscale distances. *Nat. Nanotech.* **16**, 1337–1341 (2021). doi.org/10.1038/s41565-021-00983-4

34. Y. Behovits, A. L. Chekhov, S. Yu. Bodnar, O. Gueckstock, S. Reimers, Y. Lytvynenko, Y. Skourski, M. Wolf, T. S. Seifert, O. Gomonay, M. Kläui, M. Jourdan, T. Kampfrath, Terahertz Néel spin-orbit torques drive nonlinear magnon dynamics in antiferromagnetic Mn_2Au. *Nat. Commun.* **14**, 6038 (2023). Nat Commun 14, 6038 (2023).

35. H. Tomita, S. Miwa, T. Nozaki, S. Yamashita, T. Nagase, K. Nishiyama, E. Kitagawa, M. Yoshikawa, T. Daibou, M. Nagamine, T. Kishi, S. Ikegawa, N. Shimomura, H. Yoda, Y. Suzuki, Unified understanding of both thermally assisted and precessional spin-transfer switching in perpendicularly magnetized giant magnetoresistive nanopillars. *Appl. Phys. Lett.* **102**, 042409 (2013). doi:10.1063/1.4789879

36. K. Garello, C. O. Avci, I. M. Miron, M. Baumgartner, A. Ghosh, S. Auffret, O. Boulle, G. Gaudin, P. Gambardella, Ultrafast magnetization switching by spin-orbit torques. *Appl. Phys. Lett.* **105**, 212402 (2014). doi:10.1063/1.4902443

37. S. Shi, Y. Ou, S. V. Aradhya, D. C. Ralph, R. A. Buhrman, Fast Low-Current Spin-Orbit-Torque Switching of Magnetic Tunnel Junctions through Atomic Modifications of the Free-Layer Interfaces. *Phys. Rev. Appl.* **9**, 011002 (2018). doi:10.1103/PhysRevApplied.9.011002

38. H. Honjo, T. V. A. Nguyen, T. Watanabe, T. Nasuno, C. Zhang, T. Tanigawa, S. Miura, H. Inoue, M. Niwa, T. Yoshiduka, Y. Noguchi, M. Yasuhira, A. Tamakoshi, M. Natsui, Y. Ma, H. Koike, Y. Takahashi, K. Furuya, H. Shen, S. Fukami, H. Sato, S. Ikeda, T. Hanyu,

H. Ohno, T. Endoh, “First demonstration of field-free SOT-MRAM with 0.35 ns write speed and 70 thermal stability under 400°C thermal tolerance by canted SOT structure and its advanced patterning/SOT channel technology”, *2019 IEEE International Electron Devices Meeting (IEDM)*, San Francisco, CA, USA, 2019, pp. 28.5.1-28.5.4. doi:10.1109/IEDM19573.2019.8993443

39. C. Zhang, Y. Takeuchi, S. Fukami, H. Ohno, Field-free and sub-ns magnetization switching of magnetic tunnel junctions by combining spin-transfer torque and spin–orbit torque. *Appl. Phys. Lett.* **118**, 092406 (2021). doi:10.1063/5.0039061

40. See the supplementary materials.

41. J. Yoon, Y. Takeuchi, R. Itoh, S. Kanai, S. Fukami, H. Ohno, Crystal orientation and anomalous Hall effect of sputter-deposited non-collinear antiferromagnetic Mn_3Sn thin films. *Appl. Phys. Express* **13**, 013001 (2020). doi:10.7567/1882-0786/ab5874

42. S. Nakatsuji, N. Kiyohara, T. Higo, Large anomalous Hall effect in a non-collinear antiferromagnet at room temperature. *Nature* **527**, 212–215 (2015). doi:10.1038/nature15723

43. Y. Sato, Y. Takeuchi, Y. Yamane, J.-Y. Yoon, S. Kanai, J. Ieda, H. Ohno, S. Fukami, Thermal stability of non-collinear antiferromagnetic Mn_3Sn nanodot. *Appl. Phys. Lett.* **122**, 122404 (2023). doi:10.1063/5.0135709

44. G. Q. Yan, S. Li, H. Lu, M. Huang, Y. Xiao, L. Wernert, J. A. Brock, E. E. Fullerton, H. Chen, H. Wang, C. R. Du, Quantum Sensing and Imaging of Spin–Orbit-Torque-Driven Spin Dynamics in the Non-Collinear Antiferromagnet Mn_3Sn. *Adv. Mater.* **34**, 2200327 (2022). doi:10.1002/adma.202200327

45. Y. Yang, R. B. Wilson, J. Gorchon, C.-H. Lambert, S. Salahuddin, J. Bokor, Ultrafast magnetization reversal by picosecond electrical pulses. *Sci. Adv.* **3**, e1603117 (2017). doi:10.1126/sciadv.1603117

46. Y. Shiota, T. Nozaki, F. Bonell, S. Murakami, T. Shinjo, Y. Suzuki, Induction of coherent magnetization switching in a few atomic layers of FeCo using voltage pulses. *Nat. Mater.* **11**, 39–43 (2012). doi:10.1038/nmat3172

47. S. Kanai, M. Yamanouchi, S. Ikeda, Y. Nakatani, F. Matsukura, H. Ohno, Electric field-induced magnetization reversal in a perpendicular-anisotropy CoFeB-MgO magnetic tunnel junction. *Appl. Phys. Lett.* **101**, 122403 (2012). doi.org/10.1063/1.4753816

48. Y. Wang, T. Taniguchi, P.-H. Lin, D. Zicchino, A. Nickl, J. Sahliger, C.-H. Lai, C. Song, H. Wu, Q. Dai, C. H. Back, Time-resolved detection of spin–orbit torque switching of magnetization and exchange bias. *Nat. Electron.* **5**, 840–848 (2022). doi:10.1038/s41928-022-00870-3

49. Q. Yang, D. Han, S. Zhao, J. Kang, F. Wang, S.-C. Lee, J. Lei, K.-J. Lee, B.-G. Park, H. Yang, Field-free spin–orbit torque switching in ferromagnetic trilayers at sub-ns timescales. *Nat. Commun.* **15**, 1814 (2024). doi.org/10.1038/s41467-024-46113-1

50. K. Cai, Z. Zhu, J. M. Lee, R. Mishra, L. Ren, S. D. Pollard, P. He, G. Liang, K. L. Teo, H. Yang, Ultrafast and energy-efficient spin–orbit torque switching in compensated ferrimagnets. *Nat. Electron.* **3**, 37–42 (2020). doi:10.1038/s41928-019-0345-8

51. D.-Y. Zhao, P.-B. He, M.-Q. Cai, Terahertz oscillation in a noncollinear antiferromagnet under spin-orbit torques. *Phys. Rev. B* **104**, 214423 (2021). doi:10.1103/PhysRevB.104.214423

52. S. I. Kiselev, J. C. Sankey, I. N. Krivorotov, N. C. Emley, R. J. Schoelkopf, R. A. Buhrman, D. C. Ralph, Microwave oscillations of a nanomagnet driven by a spin-polarized current. *Nature* **425**, 380–383 (2003). doi:10.1038/nature01967

53. A. A. Tulapurkar, Y. Suzuki, A. Fukushima, H. Kubota, H. Maehara, K. Tsunekawa, D. D. Djayaprawira, N. Watanabe, S. Yuasa, Spin-torque diode effect in magnetic tunnel junctions. *Nature* **438**, 339–342 (2005). doi:10.1038/nature04207

54. O. V. Gomonay, V. M. Loktev, Using generalized Landau-Lifshitz equations to describe the dynamics of multi-sublattice antiferromagnets induced by spin-polarized current. *Low Temp. Phys.* **41**, 698–704 (2015). doi:10.1063/1.4931648

55. Y. Yamane, O. Gomonay, J. Sinova, Dynamics of noncollinear antiferromagnetic textures driven by spin current injection. *Phys. Rev. B* **100**, 054415 (2019). doi:10.1103/PhysRevB.100.054415

56. T. Taniguchi, S. Mitani, M. Hayashi, Critical current destabilizing perpendicular magnetization by the spin Hall effect. *Phys. Rev. B* **92**, 024428 (2015). doi:10.1103/PhysRevB.92.024428

57. C. Zhang, S. Fukami, K. Watanabe, A. Ohkawara, S. DuttaGupta, H. Sato, F. Matsukura, H. Ohno, Critical role of W deposition condition on spin-orbit torque induced magnetization switching in nanoscale W/CoFeB/MgO. *Appl. Phys. Lett.* **109**, 192405 (2016). doi:10.1063/1.4967475

58. Data for: Y. Takeuchi, Y. Sato, Y. Yamane, J.-Y. Yoon, Y. Kanno, T. Uchimura, K. V. D. Zoysa, J. Han, S. Kanai, J. Ieda, H. Ohno, S. Fukami, Electrical coherent driving of chiral antiferromagnet, NIMS Materials Data Repository (MDR); https://doi.org/10.48505/nims.5415

Acknowledgments:
We thank Y. Nakano, T. Tanno, I. Morita, R. Ono, M. Musha, H. Kodaira, F. Shibata, S. Kasai, and S. Mitani for their technical supports and helpful discussions.

Funding:
JSPS Kakenhi Grant No. 19H05622 (SF, JI, SK)
JSPS Kakenhi Grant No. 21J23061 (JYY)
JSPS Kakenhi Grant No. 22K14558 (YT)
JSPS Kakenhi Grant No. 22KK0072 (YY, YT)
JSPS Kakenhi Grant No. 22KF0035 (SF, JH)
JSPS Kakenhi Grant No. 23KJ0216 (TU)
JSPS Kakenhi Grant No. 24KJ0432 (YS)
JSPS Kakenhi Grant No. 24K16999 (JH)
JSPS Kakenhi Grant No. 24H00039 (SF, YT, YY, SK, JI)
JST PRESTO Grant No. JPMJPR24H6 (YT)
JST PRESTO Grant No. JPMJPR21B2 (SK)
MEXT Initiative to Establish Next-Generation Novel Integrated Circuits Centers (X-NICS) Grant No. JPJ011438 (SF)
Iketani Science and Technology Foundation No. 0331108-A (YY, YT, JYY)
Iketani Science and Technology Foundation No. 0361247-A (YT, YY)
Casio Science and Technology Foundation No. 39-11 and 40-4 (YT)
Seiko Instruments Advanced Technology Foundation, Research Grants 2024 (YT)
Research Institute of Electrical Communication, Cooperative Research Projects (SF)

Author contributions:
Conceptualization: YT, YY, SF
Methodology: YT, YY, SF
Software: YT, YS, YY
Validation: YT, YS, YY
Formal analysis: YT, YS, YY, SF
Investigation: YT, YS, YY, YK
Resources: YT, YS, YY, JYY, YK, TU, KVDZ, SK, HO, SF
Data curation: YT, YS, YY
Writing – original draft: YT, YY, JH, JI, SF
Writing – review & editing: YT, YS, YY, JYY, YK, TU, KVDZ, JH, SK, JI, HO, SF
Visualization: YT, YS, YY, SF
Supervision: HO, SF
Project administration: YT, YY, HO, SF
Funding acquisition: YT, YS, YY, JYY, TU, JH, SK, JI, HO, SF

Competing interests: Authors declare that they have no competing interests.

Data and materials availability: All of the data needed to evaluate the conclusions in this work are available in the main text or the supplementary materials and have also been deposited to the NIMS Materials Data Repository (MDR) (58).

Supplementary Materials

Materials and Methods
Supplementary Text

Figs. S1 to S14

Figure legends:

Fig. 1. Sample layout and measurement system. The system is used for electrical control of coherent antiferromagnetic chiral-spin rotation in Mn_3Sn nanodot. (**A**) Illustration of Hall device with a Mn_3Sn nanodot and a W/Ta channel. (**B**) Scanning electron microscopy image of a fabricated Hall device. (**C**) Schematic of the Hall device, coplanar waveguide, and measurement system. (**D**) A transmitted waveform of the applied pulse of 0.1 ns. The measurement is performed at room temperature.

Fig. 2. Field- and SOT-induced switching of a Mn_3Sn nanodot. (**A**) R_H-H_Z curve of prepared Mn_3Sn nanodot. (**B**), (**C**) In-plane magnetic field dependence of R_H-J_{HM} curves for pulse width τ of 100 ms and 0.1 ns, respectively. (**D**) R_H-J_{HM} curves for various τ. Both R_H-H and R_H-J_{HM} curves are measured for Mn_3Sn nanodot with a nominal diameter of 200 nm. The measurement is performed at room temperature.

Fig. 3. Switching probability and field-free switching. (**A**)-(**D**) P versus J_{HM} for various τ. (**E**)-(**H**) 2D mapping of P versus J_{HM} and τ for various in-plane magnetic field H_x. The red and blue arrows above (E) point at switched and switched-back regions through coherent chiral-spin rotation, respectively. The numbers without (with) the prime symbol denote 180° coherent chiral spin rotation being completed one, three, …, $2N$-1 (two, four, …, $2N$) times. (**I**), (**J**) schematic illustration of switching and switching-back process through controlling the coherent chiral-spin rotation of Mn_3Sn by short current pulse of $\tau \sim (2N+1)\ \tau_{180t}$ and $2N\tau_{180}$, respectively. θ and τ_{180} denote the angle of the antiferromagnetic order parameter in the kagome plane and the time period for 180° rotation under the given J_{HM}, respectively. (**K**) Pulse number dependence of Hall

resistance in Mn_3Sn nanodot at zero magnetic field. Here, current pulse J_{HM} = 112 MA cm^{-2} and τ = 0.1 ns is applied to the Hall devices. The measurement is performed at room temperature.

Fig. 4. Relationship among pulse width, amplitude and switching properties. (**A**) τ dependence of switching current density J_C for various H_x. (**B**) P vs. τ for J_{HM} = 104 MA cm^{-2}. (**C**) Current dependence of chiral-spin rotation frequency f_{rot}. No magnetic field is applied for (B) and (C). More details on f_{rot} , including the definition of the error bars, are found in Section S10 of (*40*).

Fig. 5. Numerical calculation of switching current. (A)-(C) Calculated switching current density versus Gilbert damping constant in chiral antiferromagnet and ferromagnet for τ = 1, 0.1, and 0.01 ns, respectively.

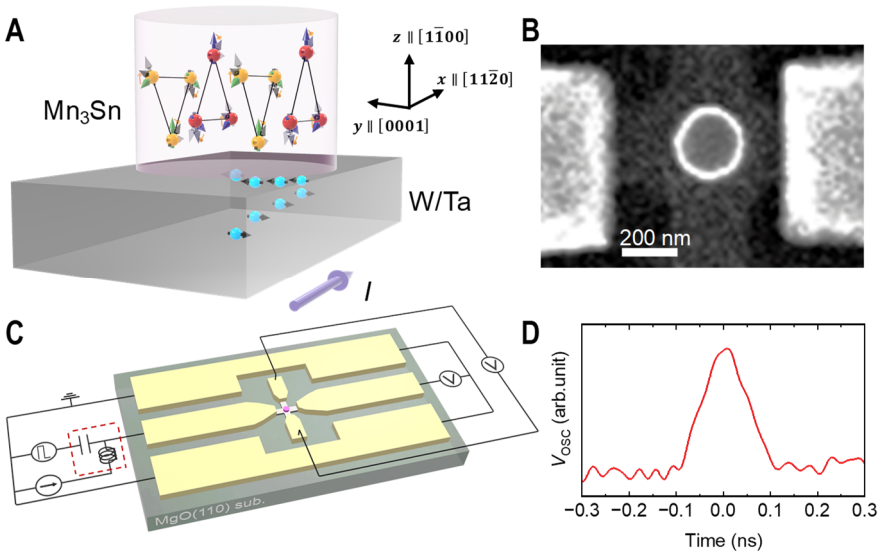

Fig. 1, Takeuchi et al.

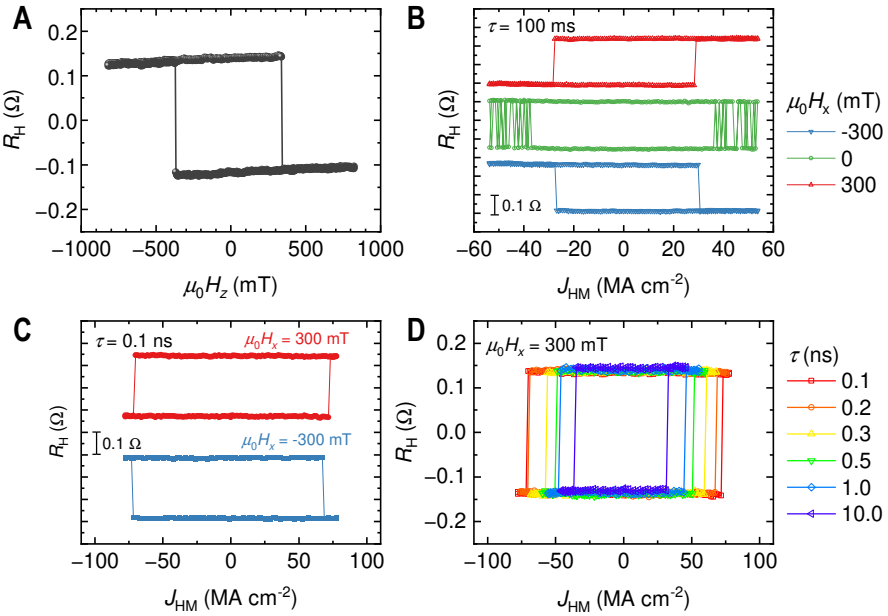

Fig. 2, Takeuchi et al.

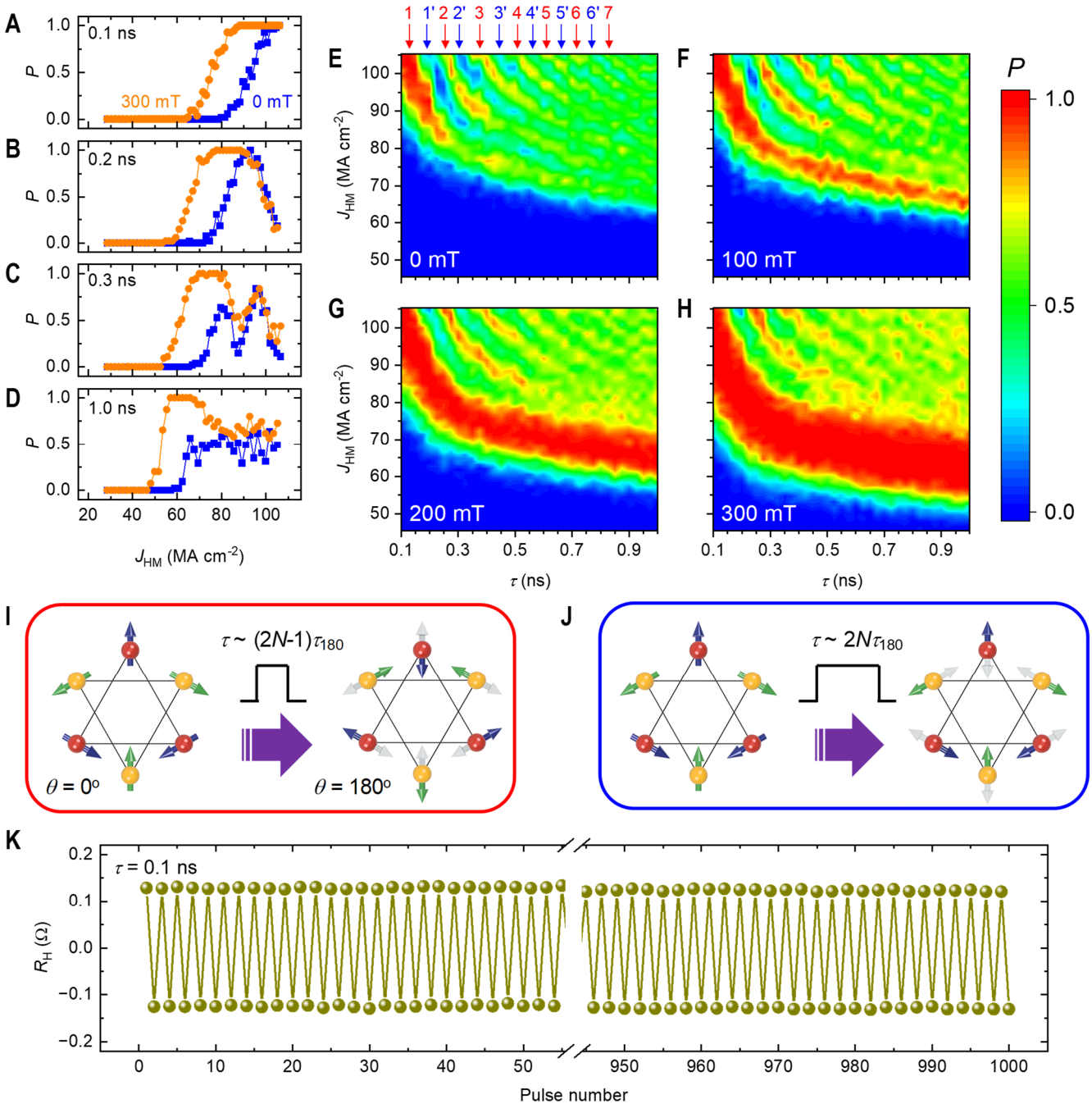

Fig. 3, Takeuchi et al.

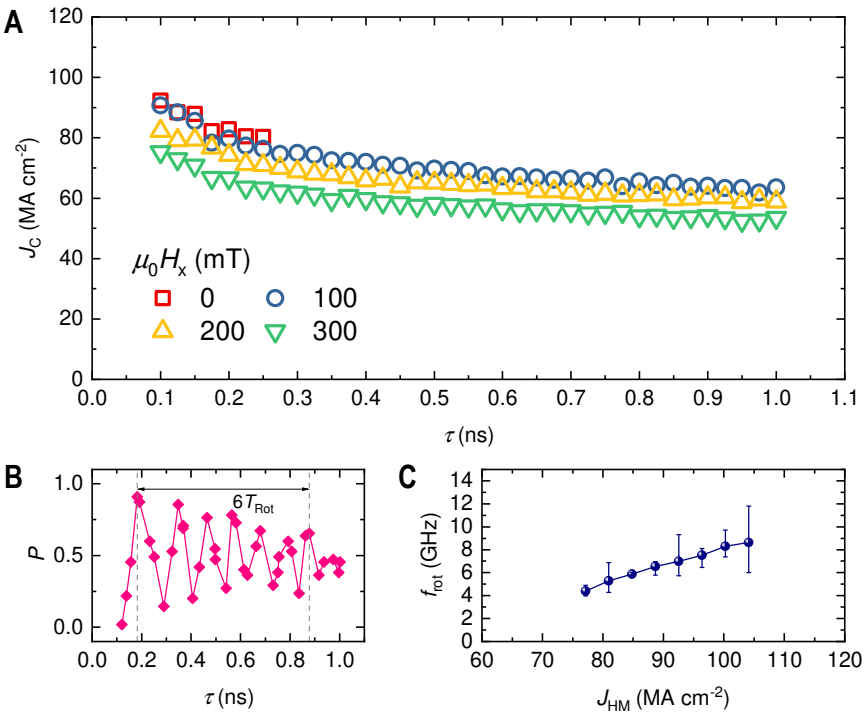

Fig. 4, Takeuchi et al.

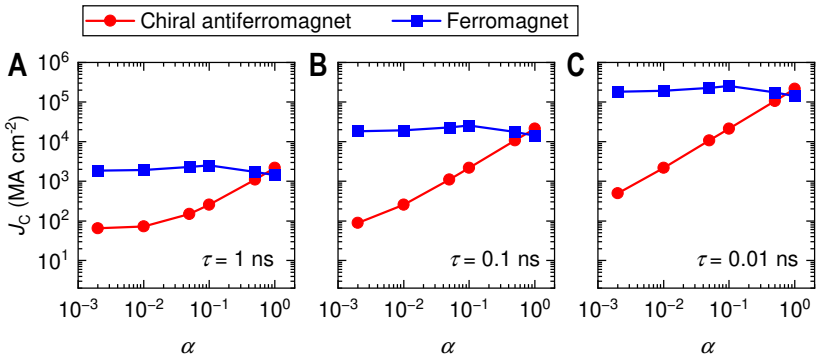

Fig. 5, Takeuchi et al.

Science
AAAS

Supplementary Materials for

Electrical coherent driving of chiral antiferromagnet

Yutaro Takeuchi, Yuma Sato, Yuta Yamane, Ju-Young Yoon, Yukinori Kanno, Tomohiro Uchimura, K. Vihanga De Zoysa, Jiahao Han, Shun Kanai, Jun'ichi Ieda, Hideo Ohno, and Shunsuke Fukami

Corresponding author: takeuchi.yutaro@nims.go.jp (Y.T.); yutaymn@tohoku.ac.jp (Y.Y.); s-fukami@tohoku.ac.jp (S.F.);

The PDF file includes:

Materials and Methods

Samples

The stack was deposited on MgO(110) single crystal substrate by magnetron sputtering. The MgO film layer was deposited by radio-frequency magnetron sputtering and other layers were deposited by DC magnetron sputtering. Mn_3Sn film is deposited through the co-sputtering of Mn and Sn targets. The deposited stack consists of, from the substrate side, W(2 nm) / Ta(3 nm) / Mn_3Sn(20 nm) / MgO(1.3 nm) / Ru(1 nm). MgO was deposited at room temperature, whereas W, Ta, Mn_3Sn, and Ru were deposited at 400 ºC on a heated stage. The base pressure of sputtering chambers was less than 1.0×10^{-6} Pa. The film was annealed at 500 ºC for an hour in a vacuum after the deposition. The Mn composition in the Mn_3Sn layer is obtained to be 76.8% by inductively coupled plasma-mass spectrometry. The prepared stack was processed into nanodot Hall devices. First, the dot was patterned by electron beam lithography and Ar ion milling. During the milling, we monitored the secondary ion mass spectra and stopped the milling when the Sn signal from the Mn_3Sn layer disappeared. After the milling, Ta(3 nm) / Ru(1 nm) was deposited using DC magnetron sputtering to protect W(2 nm) / Ta(3 nm) underlayers from oxidation. Next, the W / Ta / Ru channel was formed by electron beam lithography and Ar ion milling. Then, electrodes made of Cr(5 nm) / Au(100 nm) film, attached to the channel, were formed using electron beam lithography and liftoff. Finally, the coplanar waveguide and contact pads for probing Hall voltage, made of Cr(5 nm) / Au(100 nm), were formed using photolithography and liftoff. After fabricating Hall dot devices, we captured their images using a scanning electron microscope (Fig.1B of the main text). The standard deviation between the actual and nominal device sizes is obtained to be about 15 nm.

Experimental Setup

The structure properties of the prepared stack were characterized by the X-ray diffraction measurement using a Bruker X-ray diffractometer. A Cu-Kα1 X-ray was used in the diffractometer with a wavelength of 1.54056 Å. All electrical measurements were performed at room temperature using a probing station with the measurement circuit depicted in Fig. 1C. The out-of-plane or in-plane magnetic field can be applied by electromagnets in the probing station. A current source (Yokogawa; Model GS200) was used to apply DC current into the channel and the Hall voltage was measured by a nano-voltmeter (Keithley; Model 2182A). A DC current with a magnitude of 100 μA was supplied when measuring the Hall voltage of the nanodot device. Short pulse voltages of 0.1-10 ns were applied from a pulse generator (Agilent; Model 81134). Transmitted waveforms of the injected pulse are monitored through an oscilloscope (Agilent; Model DSOX93204A) with an internal impedance of 50 Ω. After the electrical switching of Mn_3Sn, a pulse current of 0.1 s was applied from the current source to initialize the spin ordering.

Supplementary Text

S1. Structure properties of Mn_3Sn film

To characterize the structure properties of the prepared stack, we perform the X-ray diffraction (XRD) measurement using a Bruker X-ray diffractometer. Figure S1A shows the obtained pattern of out-of-plane XRD measurement in the blanket film. The $(1\bar{1}00)$ and $(3\bar{3}00)$ super lattice peaks $D0_{19}$-Mn_3Sn are observed in addition to the $(2\bar{2}00)$ and $(4\bar{4}00)$ fundamental peaks, indicating the $(1\bar{1}00)$ (M-plane) orientation of $D0_{19}$-ordered phase, which is consistent with previous studies (*28*, *41*). The ϕ scan patterns for MgO substrate and the Mn_3Sn layer are

shown in Fig.S1B, indicating the epitaxial growth of M-plane ordered Mn_3Sn. The epitaxial relationship can be described as $MgO(110)[001] \parallel Mn_3Sn(1\bar{1}00)[0001]$.

S2. Transmitted waveforms of sub-ns ~ ns pulse voltage

To evaluate the magnitude of applied pulse current flowing into the nanodot Hall bar device, transmitted waveforms of the pulse are measured by the oscilloscope. Figure S2 shows measured waveforms for various nominal pulse widths τ and input voltage in the pulse generator. We confirm that the amplitude of transmitted pulse voltage V_{OSC} decreases at shorter τ. The magnitude of pulse current I can be obtained as V_{OSC}/R_{OSC}, where R_{OSC} (= 50 Ω) denotes the internal impedance of the oscilloscope.

S3. Evaluation of shunt current in nanodot device

We prepared nanoscale Hall devices with W(2 nm) / Ta(6 nm) / Ru(1 nm) channels and nanodots consisting of W(2 nm) / Ta(3 nm) / Mn_3Sn(20 nm) / MgO(1.3 nm) / Ru(1 nm). Figure S3A is the schematic illustration of the prepared device. We note that Ta(3 nm) / Ru(1 nm) films are deposited after milling Mn_3Sn nanodots. To evaluate the current density flowing into W(2 nm)/Ta(3 nm) layers under Mn_3Sn nanodots, we consider an electric circuit as shown in Fig.S3B. Here, R_{Ch} denotes the resistance of channel regions, R_{Dot} the resistance of dot, and R_{Int} the resistance of intersection regions of W/Ta/Ru channel and Hall probe. Considering the parallel resistance model, the conductance of each region can be approximately estimated as

$$\frac{1}{R_{\mathrm{Ch}}} \sim \frac{w_{\mathrm{Ch}}}{l_{\mathrm{Ch}}}\left(\frac{t_{\mathrm{W}}^{\mathrm{Ch}}}{\rho_{\mathrm{W}}}+\frac{t_{\mathrm{Ta}}^{\mathrm{Ch}}}{\rho_{\mathrm{Ta}}}+\frac{t_{\mathrm{Ru}}^{\mathrm{Ch}}}{\rho_{\mathrm{Ru}}}\right), \tag{S1A}$$

$$\frac{1}{R_{\mathrm{Dot}}} \sim \left(\frac{t_{\mathrm{W}}^{\mathrm{Dot}}}{\rho_{\mathrm{W}}}+\frac{t_{\mathrm{Ta}}^{\mathrm{Dot}}}{\rho_{\mathrm{Ta}}}+\frac{t_{\mathrm{Mn_3Sn}}^{\mathrm{Dot}}}{\rho_{\mathrm{Mn_3Sn}}}\right), \tag{S1B}$$

$$\frac{1}{R_{\mathrm{Cross}}} \sim \frac{w_{\mathrm{Int}}}{l_{\mathrm{Int}}}\left(\frac{t_{\mathrm{W}}^{\mathrm{Channel}}}{\rho_{\mathrm{W}}}+\frac{t_{\mathrm{Ta}}^{\mathrm{Channel}}}{\rho_{\mathrm{Ta}}}+\frac{t_{\mathrm{Ru}}^{\mathrm{Channel}}}{\rho_{\mathrm{Ru}}}\right), \tag{S1A}$$

where w_{X} is the width of X region, l_{X} the length of X region, $t_{\mathrm{Y}}^{\mathrm{X}}$ the thickness of Y layer in X region, and ρ_{Y} the resistivity of Y layer. Here, we assume the square-shaped dot with the effective length of $\frac{\sqrt{\pi}}{2}D$. Following this assumption, w_{Int} and l_{Int} can be expressed as $\frac{w_{\mathrm{Channel}}-\frac{\sqrt{\pi}}{2}D}{2}$ and $\frac{w_{\mathrm{Probe}}-\frac{\sqrt{\pi}}{2}D}{2}$, respectively. Here, the resistivities of each layer are assumed as ρ_W = 60.2 μΩcm, ρ_{Ta} = 122.8 μΩcm, ρ_{Mn_3Sn} = 333.3 μΩcm, and ρ_{Ru} = 36.2 μΩcm (*28*) to evaluate the device resistance. The procedure for evaluating the resistivities of W, Ta, and Mn_3Sn is given in Supplementary Text 4. Due to the oxidation of Ta layer after milling Mn_3Sn nanodot, we assume that 3-nm-thick Ta layer is insulated in the W(2 nm) / Ta(6 nm) / Ru(1 nm) channel and intersection regions. Using eqs. (S1A), (S1B), and (S1C), we evaluate the shunt current density flowing W/Ta layer in the dot region.

S4. Evaluation of the layer resistivities

To evaluate the layer resistivities in the stacks, we measure the sheet resistance of blanket films by a four-probe method. We prepared three series of stacks consisting of, from substrate side, W(t_W)/MgO(1.3 nm)/Ru(1 nm) (Series A), W(2 nm)/Ta(t_{Ta})/MgO(1.3 nm)/Ru(1 nm) (Series B), and W(2 nm)/Ta(3 nm)/Mn_3Sn(t_{Mn3Sn})/MgO(1.3 nm)/Ru(1 nm) (Series C) by magnetron sputtering, where t_W, t_{Ta}, and t_{Mn3Sn} denote the layer thicknesses of W, Ta, and Mn_3Sn, respectively. All films are deposited on MgO(110) substrate. The dependencies of the sheet conductance G_S on the layer thicknesses for series A, B, and C are summarized in Fig.4S. The resistivities are determined through the linear fitting of G_S versus the layer thicknesses. We obtain the layer resistivities as ρ_W = 60.2 μΩcm, ρ_{Ta} = 122.8 μΩcm, and ρ_{Mn_3Sn} = 333.3 μΩcm, which are used to estimate the shunt current in the nanodot devices.

S5. Measurement of switching probability in Mn_3Sn nanodot

In Fig.3A-H, the results of SOT-induced switching probability P as a function of current density J_{HM}, pulse width τ, and in-plane magnetic field H_x are displayed. Here, we describe the procedure for measuring P in chiral-antiferromagnetic Mn_3Sn nanodot. First, the antiferromagnetic chiral-spin structure is initialized to low R_H state by applying pulse current with τ of 100 ms and J_{HM} = 42 MA cm^{-2} under $\mu_0 H_x$ = 300 mT, followed by measuring Hall resistance R_H under DC current density of 3.8 MA cm^{-2}. The 100 ms-pulse and DC current is generated from the current source connected to the DC port of the bias-tee (see also Fig.1C of the main text). Next, current pulse with the opposite polarity is applied to induce the switching under applied $\mu_0 H_x$ of 0, 100, 200, or 300 mT. Then, R_H is measured to check whether the spin structure of Mn_3Sn nanodot is switched. We repeat the measurement at least 50 times for each J_{HM}, τ, and H_x to evaluate P. Figure S5A-C show the distributions of R_H versus J_{HM} after the injection of single pulse with τ of 0.10, 0.15, and 1.0 ns, respectively, under no external magnetic field. R_H exhibits the binarized states of high and low resistance. Figure S5D displays the histogram of measured R_H after initialization, which confirms that there are no initialize errors. The two-dimensional color maps of Fig. 3E-H are displayed with linearly interpolated values of experimental P versus J_{HM} and τ.

S6. Calculation of chiral antiferromagnetic dynamics and switching phase diagram

We model Mn_3Sn by a three-sublattice antiferromagnet, with each of the magnetic sublattices A, B and C carrying a common saturation magnetization M_S. The classical unit vector $\boldsymbol{m}_A$ represents the sublattice magnetization direction in the sublattice A, and similarly defined are $\boldsymbol{m}_B$ and $\boldsymbol{m}_C$. Now we introduce antiferromagnetic order parameters (*54*).

$$\boldsymbol{n}_1 = \frac{\boldsymbol{m}_A + \boldsymbol{m}_B - 2\boldsymbol{m}_C}{3\sqrt{2}}, \qquad \boldsymbol{n}_2 = \frac{-\boldsymbol{m}_A + \boldsymbol{m}_B}{\sqrt{6}}.$$

When $|\boldsymbol{m}| = \frac{1}{3}|\boldsymbol{m}_A + \boldsymbol{m}_B + \boldsymbol{m}_C| \ll 1$, i.e., the sublattice magnetizations make a nearly perfect triangular structure, it can be shown directly from the above definitions that $\boldsymbol{n}_1 \cdot \boldsymbol{n}_2 \simeq 0$ and $|\boldsymbol{n}_1| \simeq |\boldsymbol{n}_2| \simeq \frac{1}{\sqrt{2}}$. As $\boldsymbol{y} \cdot \boldsymbol{n}_1 \times \boldsymbol{n}_2 < 0$ for the inverse triangular spin structure in Mn_3Sn, it suffices to track either $\boldsymbol{n}_1$ or $\boldsymbol{n}_2$ for describing the time evolution of the antiferromagnetic order. In the simulation below, we start from an initial state with $\boldsymbol{n}_1 \parallel +\boldsymbol{z}$, and the magnetic state is considered as "switched" if $\boldsymbol{n}_1 \parallel -\boldsymbol{z}$ is reached after an electric current pulse is applied and then turned off. We assume spatial homogeneity in the magnetic structure and the magnetic energy density given by

$$u_{\mathrm{AF}} = J_{\mathrm{ex}}(\boldsymbol{m}_A \cdot \boldsymbol{m}_B + \boldsymbol{m}_B \cdot \boldsymbol{m}_C + \boldsymbol{m}_C \cdot \boldsymbol{m}_A) - D\boldsymbol{y} \cdot (\boldsymbol{m}_A \times \boldsymbol{m}_B + \boldsymbol{m}_B \times \boldsymbol{m}_C + \boldsymbol{m}_C \times \boldsymbol{m}_A)$$
$$-K \sum_{\eta=A,B,C} \left(\boldsymbol{e}_K^{\eta} \cdot \boldsymbol{m}_{\eta}\right)^2 - \frac{K_z}{3} \sum_{\eta=A,B,C} \left(\boldsymbol{e}_{K_z}^{\eta} \cdot \boldsymbol{m}_{\eta}\right)^2,$$

where J_{ex} (>0) is the antiferromagnetic exchange coupling constant, $D(>0)$ is the homogeneous Dzyaloshinskii-Moriya coupling constant, $K(>0)$ is the magnetic anisotropy constant originating from the local crystalline symmetry with $\boldsymbol{e}_K^{\eta}$ being the unit vector along the easy axis for $\boldsymbol{m}_{\eta}$, and $K_z(>0)$ phenomenologically describes the uniaxial anisotropy for $\boldsymbol{n}_1$ along the z direction with $\boldsymbol{e}_{K_z}^{\eta}$ the unit vector representing the corresponding easy axis for $\boldsymbol{m}_{\eta}$. Here we set the x, y and z axes along $[11\bar{2}0]$, $[0001]$ and $[1\bar{1}00]$, respectively, of Mn_3Sn. The explicit expressions of $\boldsymbol{e}_K^{\eta}$ and $\boldsymbol{e}_{K_z}^{\eta}$ are; $\boldsymbol{e}_K^A = (\cos\frac{2\pi}{3}, 0, \sin\frac{2\pi}{3})$, $\boldsymbol{e}_K^B = (\cos\frac{4\pi}{3}, 0, \sin\frac{4\pi}{3})$, $\boldsymbol{e}_K^C = (1,0,0)$, $\boldsymbol{e}_{K_z}^A = (\cos\frac{\pi}{6}, 0, -\sin\frac{\pi}{6})$, $\boldsymbol{e}_{K_z}^B = (-\cos\frac{\pi}{6}, 0, -\sin\frac{\pi}{6})$, and $\boldsymbol{e}_{K_z}^C = (0,0,1)$.

The sublattice magnetizations $\boldsymbol{m}_{\eta}$ $(\eta = A, B, C)$ are assumed to obey coupled Landau-Lifshitz-Gilbert (LLG) equations,

$$\frac{\partial \boldsymbol{m}_{\eta}}{\partial t} = -\gamma \boldsymbol{m}_{\eta} \times \boldsymbol{H}_{\eta} + \alpha \boldsymbol{m}_{\eta} \times \frac{\partial \boldsymbol{m}_{\eta}}{\partial t} - \gamma \boldsymbol{m}_{\eta} \times \left(\boldsymbol{m}_{\eta} \times \boldsymbol{H}_S\right),$$

where γ is the gyromagnetic ratio, α is the Gilbert damping constant, $\boldsymbol{H}_{\eta} = -\frac{1}{M_S}\frac{\partial u}{\partial \boldsymbol{m}_{\eta}}$ is the effective magnetic field acting on $\boldsymbol{m}_{\eta}$, and $\boldsymbol{H}_S = \frac{1}{3}\frac{\hbar \vartheta J_{HM}}{2eM_S d}\boldsymbol{y}$ is the current-induced Slonczewski-like effective field with ϑ and d denoting, respectively, the spin Hall angle of the heavy metal layer and the film thickness of the Mn_3Sn layer. The factor $\frac{1}{3}$ in $\boldsymbol{H}_S$ reflects the sublattice symmetry where the spin current injected into Mn_3Sn is transferred equiprobably to each of the three magnetic sublattices.

It is challenging to experimentally measure some of the parameters, such as the local anisotropy K and the DMI constant D. However, there are theoretical relations that these parameters must satisfy (*55*). First, in order for the inverse triangular spin structure to be stable, the relation $J_{\mathrm{ex}} \gg D \gg K$ has to be satisfied. Second, the uncompensated small magnetization $\boldsymbol{m}$ is given by $|\boldsymbol{m}| \approx M_S K / J_{\mathrm{ex}}$. These relations greatly narrow down the ranges of values that K and D can take, while J_{ex} and K_z have been experimentally evaluated in Mn_3Sn nanodots (*43*), and M_S can be estimated from the magnetic moment caried by each Mn atom. Based on these reasonings, we employ the following parameter values; $\gamma = 1.76 \times 10^{11}$ $\mathrm{HzT^{-1}}$, $M_S = 0.55$ T, $J_{\mathrm{ex}} = 6.2 \times 10^7$ $\mathrm{Jm^{-3}}$, $D = 6 \times 10^6$ $\mathrm{Jm^{-3}}$, $K = 3.8 \times 10^5$ $\mathrm{Jm^{-3}}$, $K_z = 3.4 \times 10^2$ $\mathrm{Jm^{-3}}$, $\alpha = 0.002$, $d = 20$ nm, and $\vartheta = 0.033$. In the calculations shown in Fig. 5 of the main text, we use the same parameter values as here, except for α (we examine the α dependence of $J_C(\tau)$ in Fig. 5).

We investigate the current-driven dynamics of Mn_3Sn by numerically solving the Landau-Lifshitz-Gilbert equations. Displayed in Fig. S6 is the calculated switching phase diagram against the pulse amplitude J_{HM} and width τ. We find a quantitatively good agreement with the experimental result in Fig. 3E. Because of the absence of thermal effects in the calculation, the boundaries between the switched and switched-back regions are sharply defined, i.e., deterministic switching/switching-back with given (J_{HM}, τ).

S7. Pulse-shape dependence of the switching current density

Here we numerically investigate impacts of the pulse shape on $J_C(\tau)$. The same parameter values as in S6 are used, and the results are shown in Fig. S7. We take the pulse shapes so as the total amount of the spin angular momentum injected into Mn_3Sn to be kept unchanged, to examine the effects purely originating from the pulse shape.

S8. Dependence of switching on writing pulse number

As shown in Fig.3K of the main text, we demonstrate a part of the field-free switching 1,000 times by single pulse current through the control of coherent chiral-spin rotation in Mn_3Sn nanodot. This section describes the result of all-electrical switching 1,000 times in the same nanodot device. The pulse current of $\tau = 0.1$ ns and $J_{HM} = 112$ MA cm^{-2} is applied under $\mu_0 H_x = 0$ mT as well as Fig.4A of the main text. Figure S8 shows the pulse number dependence of measured R_H for pulse number ranges of 1 to 1,000. We confirm the binary switching 1,000 times in succession by single pulses with no write error, which had not been realized in previous studies using antiferromagnet-based devices.

S9. Switching current versus pulse width: Comparison with other ferromagnetic and ferrimagnetic systems

The SOT-induced switching current density J_C versus pulse width in Mn_3Sn nanodot τ shows a small increase rate of about 1.4 times by reducing τ from 1 to 0.1 ns [Fig.4A of the main text]. Here, we show the results of a quantitative comparison of switching current I_C versus τ between chiral antiferromagnet and ferromagnet-based devices studied in previous works. Figure S9 shows τ dependence of the switching current I_C normalized by I_C at $\tau \sim 1$ ns in chiral antiferromagnetic Mn_3Sn nanodot and other ferromagnetic nanoscale devices and ferrimagnetic wire (*35–38, 49, 50*) Type-X (*39*) and type-Y (*37–39*) denote in-plane magnetized ferromagnet (FM) / heavy metal (HM) systems whose magnetic easy axes are orthogonal and parallel to the generated spin accumulation vector, respectively. Type-Z (*36, 49*) represents FM/HM system with an out-of-plane magnetic easy axis. ϕ is an angle between the current direction and magnetic easy axis (*38*). Therefore, $\phi = 0^o$ and 90^o correspond to Type-X and Type-Y systems, respectively. SOT+STT denotes the combined systems using both SOT and spin-transfer torque (STT) induced by spin-polarized current from another magnetic layer. In the chiral antiferromagnet-based SOT device, the increase of $I_C/I_C(\tau \sim 1$ ns) by reducing τ shows smaller values than other ferromagnet systems owing to the inertial nature of antiferromagnetic excitations.

S10. Determination of the rotation frequency in chiral antiferromagnet from switching probability

To obtain the chiral-spin rotation frequency f_{rot}, we estimate the rotation period and number of oscillation peaks in evaluated switching probability P versus pulse width τ. Figure S10 shows τ dependence of P for different current densities J_{HM}. The P curves exhibit damped oscillation behavior with respect to τ. We then estimate the τ distance between the first and last peaks of the oscillation. By reducing J_{HM} from 104 to 77 MAcm^{-2}, the number of observed peaks decreases from 7 to 3, corresponding to the estimated τ distance of $12\,\tau_{180}$ and $4\,\tau_{180}$, respectively, where τ_{180} is half value of the period of coherent chiral-spin rotation. Then we evaluate the J_{HM} dependence of f_{rot} as shown in Fig.4C in the main text.

We also note that the oscillation speed appears to slightly increase with τ. It may be attributed to the effect of thermal activation and variation of the pulse shape with τ. Accordingly, the error bars in Fig. 4C are provided to represent the lower and upper limits of f_{rot}, where the lower (upper) limit is estimated from the second and first (the last and the second to the last) peaks.

S11. Dependencies of the switching current density on micromagnetic parameters

Here we numerically investigate the dependencies of the current-driven Mn_3Sn dynamics on K_z, J_{ex}, D, and K. In the following, the same parameter values as in S6 are used, unless otherwise stated. First, we show $J_c(\tau)$ in Fig. S11, where $J_c(\tau)$ is defined as the value of J_{HM} at which 180-degree switching is observed with the given τ. For a comparison, numerical results for two ferromagnetic cases (FM-1 and FM-2) and our experimental results are also shown in Fig. S11; For FM-1 we take similar parameter values to Mn_3Sn to clarify fundamental differences between the two systems, while FM-2 assumes parameter values more relevant to realistic ferromagnetic materials (details of the ferromagnetic simulation are given in S14).

Figure S12A shows $J_c(\tau = 0.1\mathrm{ns})$ and $J_c(\tau = 0.01\mathrm{ns})$ as functions of K_z for Mn_3Sn. The results for FM-1 are shown for a comparison in Fig. S12B. Given in Fig. S12C are the results in the DC limit, i.e. $J_c(\tau \to \infty)$, for Mn_3Sn. Note that, in the DC limit, what we actually observe is not 180-dgree switching but the continuous chiral spin rotation. It is seen that $J_c(\tau)$ increases monotonically with K_z, as expected.

In Fig. S13, we demonstrate the J_{ex}, D, and K dependencies of $J_c(\tau)$. A general tendency is that, as τ is decreased, the dependencies of $J_c(\tau)$ on the micromagnetic parameters become more appreciable. With the pulse as short as $\tau = 0.001$ ns, however, the dependencies on the parameters are still negligible.

S12. Numerical calculation of antiferromagnetic order dynamics in time domain

In Fig. S14, we show numerical results for the evolution of n_{1z} (the definition of the antiferromagnetic order vector $\boldsymbol{n}_1$ is given in S6) in time, under several different pulse amplitudes J_{HM}. Here, the pulse length τ is fixed to 0.1 ns. Note that the length of the vector $\boldsymbol{n}_1$ is $\approx 1/\sqrt{2}$, as can be straightforwardly shown from its definition. The threshold current densities J_{C}(τ=0.1ns) for 180-degree and 360-degree rotations are ≈89 $\mathrm{MAcm^{-2}}$ and ≈152 $\mathrm{MAcm^{-2}}$, respectively. It is seen that, except for when $J_{\mathrm{HM}} \approx J_{\mathrm{C}}$, switching is completed at around 0.1 ns after the pulse application.

S13. Connection between simulation and analytical model

We briefly touch upon the relation between the coupled LLG equations for the sublattice magnetizations $\boldsymbol{m}_\eta$ and the equation of motion for the antiferromagnetic order discussed in the main text. With the aid of the assumptions $|\boldsymbol{m}| \ll 1$ and $m_\eta^y \ll 1\ \forall\eta$, the order parameter $\boldsymbol{n}_1$ can be approximately described by a single parameter θ as $\boldsymbol{n}_1 = \frac{1}{\sqrt{2}}(\sin\theta\,, 0, \cos\theta)$. In the absence of external magnetic field, the closed equation of motion for θ can be derived at the first order of $\boldsymbol{m}$ as in the main text (*55*). with $H_E = \frac{3J_{\mathrm{ex}}}{M_S}$ and $H_K = \frac{2K_z}{3M_S}$.

S14. Numerical calculation of ferromagnetic dynamics

For a ferromagnet, we solve the LLG equation of the same form as in the last section, but for the single magnetization $\boldsymbol{m}$ instead of the sublattice magnetizations $\boldsymbol{m}_\eta$. The magnetic energy density is assumed to consist only of the uniaxial magnetic anisotropy; $u_{\mathrm{FM}} = -K_z m_z^2$. The current-induced Slonczewski-like effective field is now given by $\boldsymbol{H}_S = \frac{\hbar \vartheta J_{HM}}{2eM_S d}\boldsymbol{y}$. In Fig. 5 of the main text, we adopt $M_S = 0.55$ T, $K_z = 3.4 \times 10^2$ Jm^{-3}, $d = 20$ nm, $\vartheta = 0.033$, $\gamma = 1.76 \times 10^{11}$ HzT^{-1}, and $\mu_0|H_x| = 1$ μT. The same parameter values and $\alpha = 0.002$ are used for FM-1 in Fig. S11 and S12 (K_z is varied in the latter). For FM-2 in Fig. S11, $M_S = 1.093$ T, $K_z = 4.35 \times 10^5$ Jm^{-3}, $d = 0.6$ nm, $\vartheta = 0.4$, $\alpha = 0.002$, $\gamma = 1.76 \times 10^{11}$ HzT^{-1}, and $\mu_0|H_x| = 91$ mT (*36*).

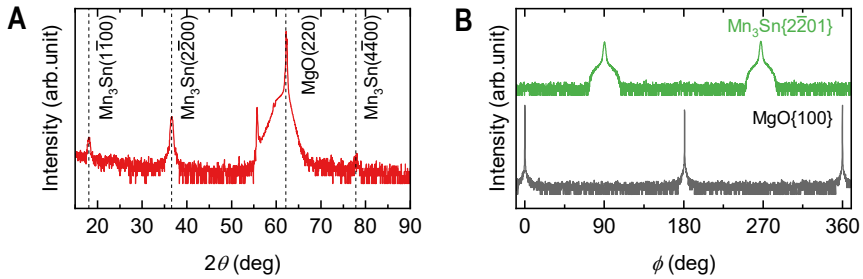

Fig. S1. Structure properties of W(2 nm) / Ta(3 nm) / Mn_3Sn(20 nm) / MgO(1.3 nm) heterostructure. (A) Out-of-plane XRD pattern of the prepared stack. (B) ϕ scan patterns for MgO{100} and $Mn_3Sn\{2\bar{2}01\}$.

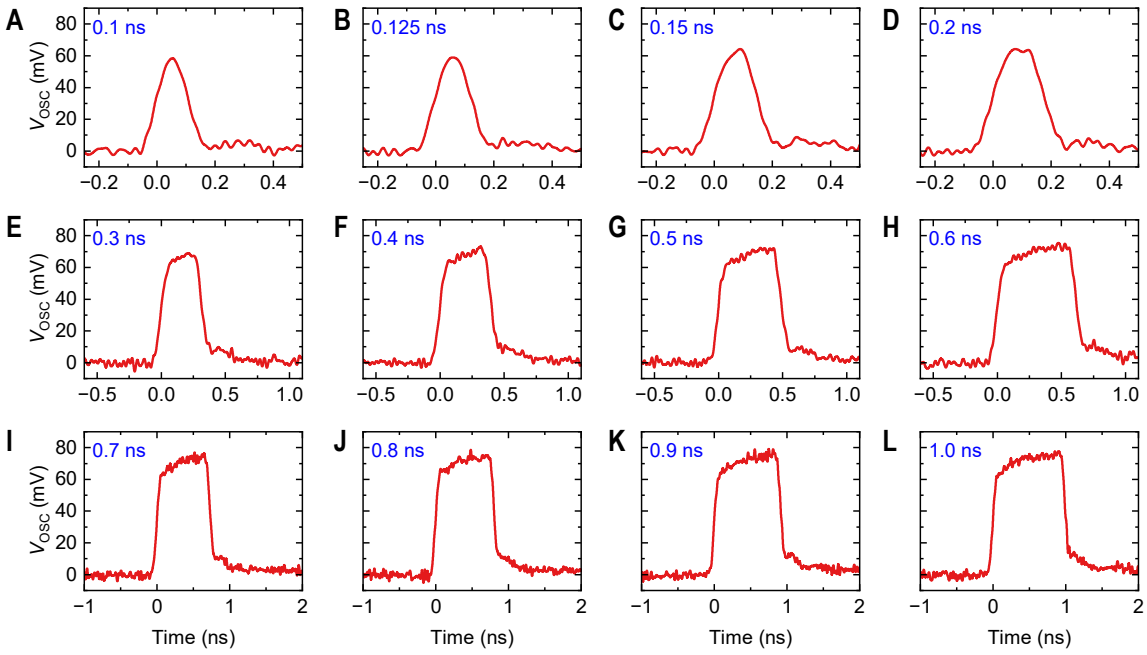

Fig. S2. Transmitted waveforms of applied pulse voltages. (A)-(L) Time dependence of transmitted voltage V_{OSC} for various pulse width. The nominal amplitude of pulse voltage is 800 mV.

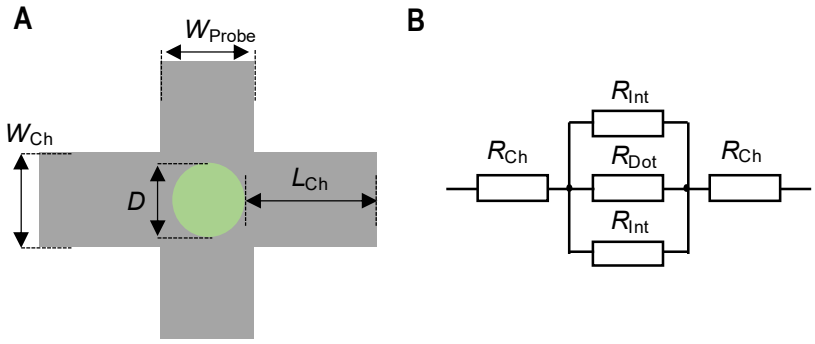

Fig. S3. Evaluation of shunt current in nanodot device. (A) Sample layout of the prepared nanodot Hall device. (B) The modelled electrical circuit for evaluation of the current density flowing into heavy metal layers under Mn_3Sn nanodot.

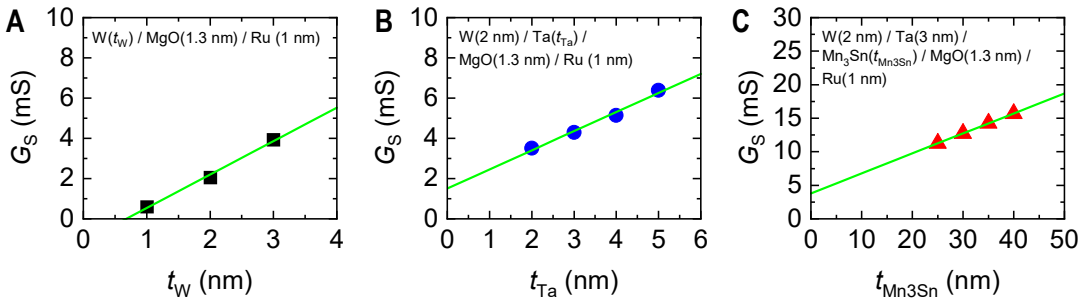

Fig. S4. Evaluation of layer resistivities. (A) t_W, (B) t_{Ta}, and (C) t_{Mn3Sn} dependence of the sheet conductance G_S in the prepared stacks. The symbols denote the experimental data and the green solid lines are the best fitting lines.

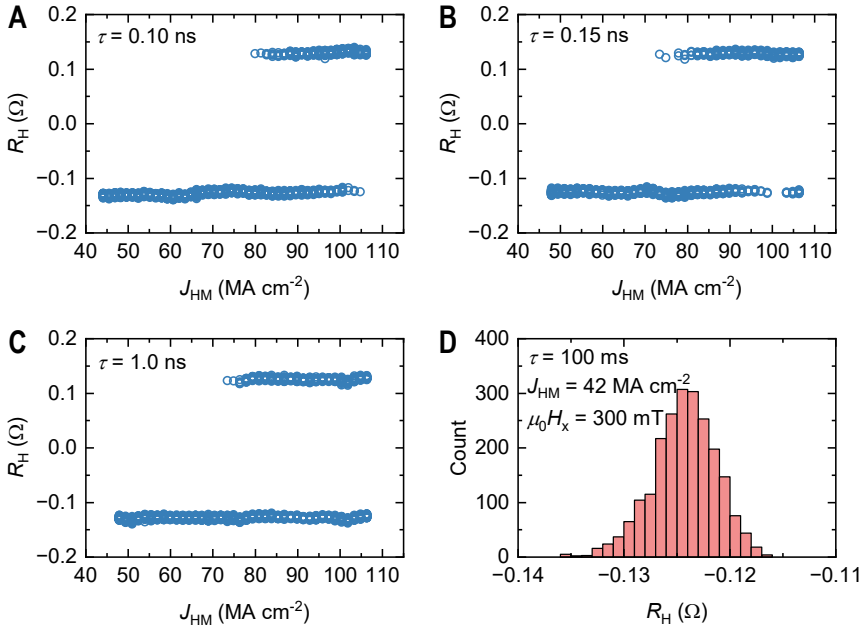

Fig. S5. Measurement of switching probability *P* versus J_{HM} and τ. (A)-(C) Distributions of Hall resistance R_H versus J_{HM} after the injection of single pulse with τ of 0.10, 0.15, and 1.0 ns, respectively, under no external magnetic field. (D) The histogram of measured R_H after initialization of Mn_3Sn nanodot.

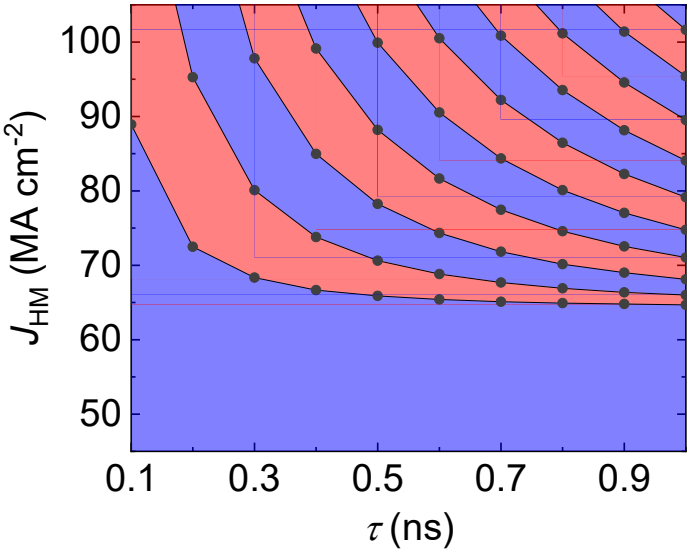

Fig. S6. Calculated switching phase diagram in chiral antiferromagnet at zero field. The black circles represent the switching current densities, numerically obtained with given pulse lengths τ (for 180º, 360º, 540º, … switching from below). The red and blue regions represent the switched and unswitched/switched-back regions, respectively.

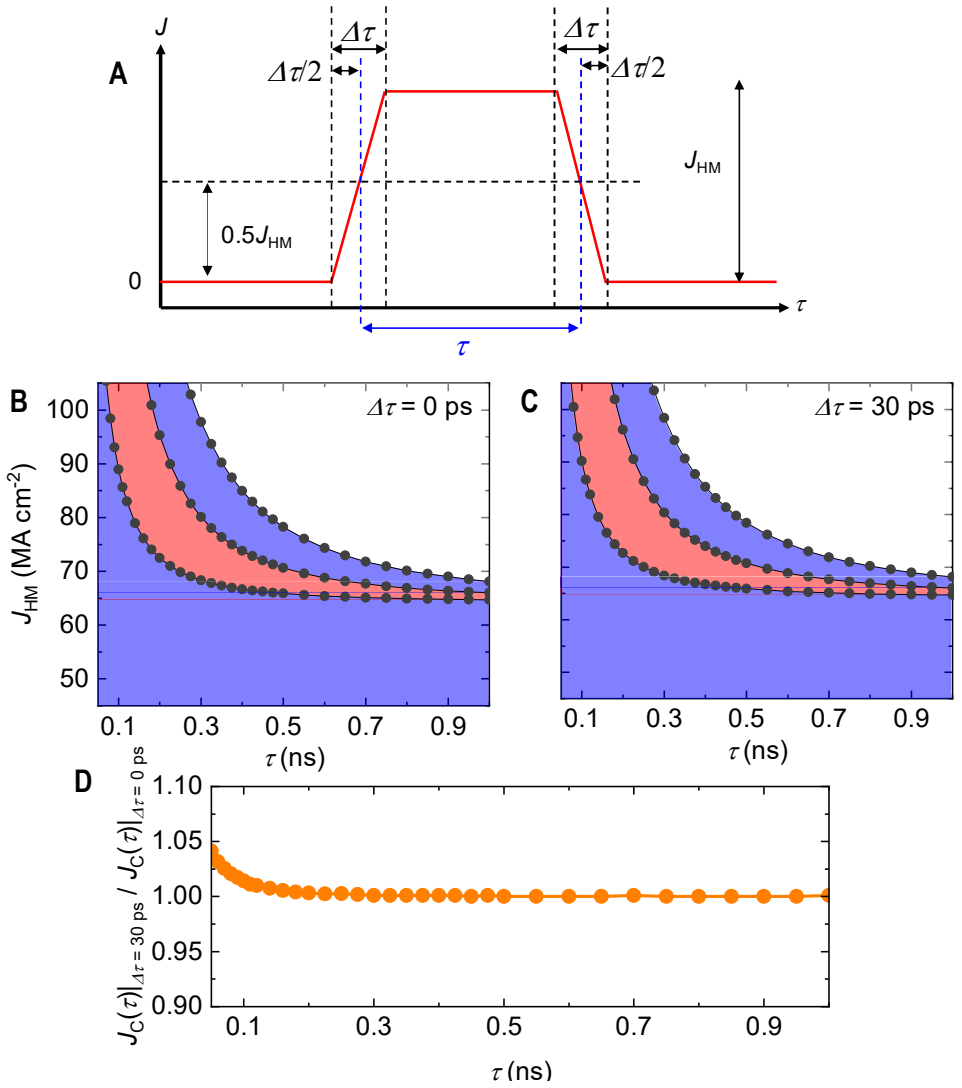

Fig. S7. Calculated pulse-shape dependence of the switching current densities. (A) The shape of the pulse current employed in the simulation here, with the rise and fall times $\Delta\tau$. The calculated switching phase diagrams for (B) $\Delta\tau$ = 0 and (C) $\Delta\tau$ = 30 ps, where the red and blue regions correspond to the switched and unswitched/switched-back regions, respectively. The white regions are uncalculated regions. (D) The ratio of $J_C(\tau)$ with $\Delta\tau$ = 30 ps to $J_C(\tau)$ with $\Delta\tau$ = 0, for 180-degree switching.

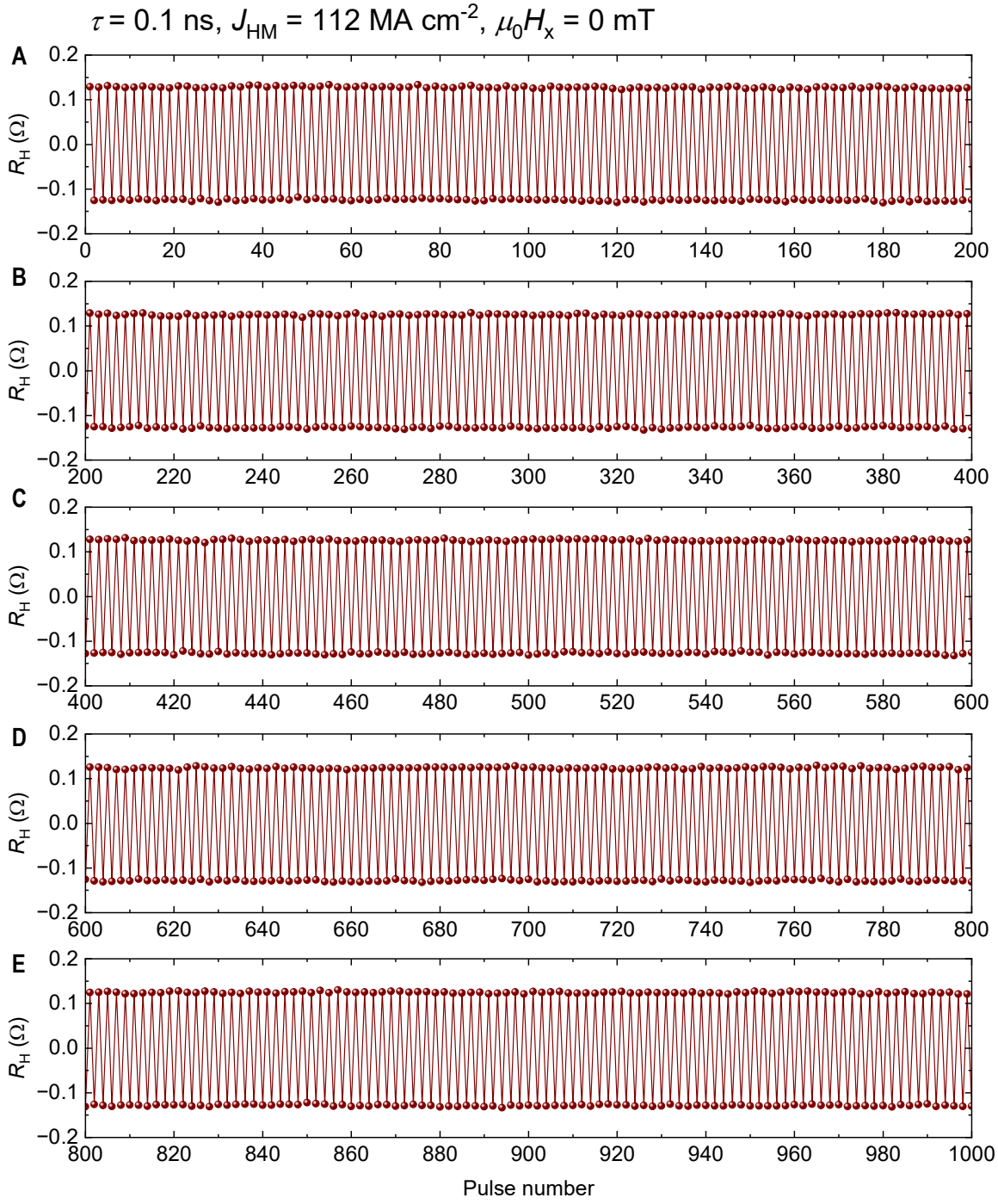

Fig. S8. Dependence of switching on writing pulse number (A)-(E) Pulse number dependence of measured R_H for pulse number ranges of 1-200, 201-400, 401-600, 601-800, and 801-1000, respectively.

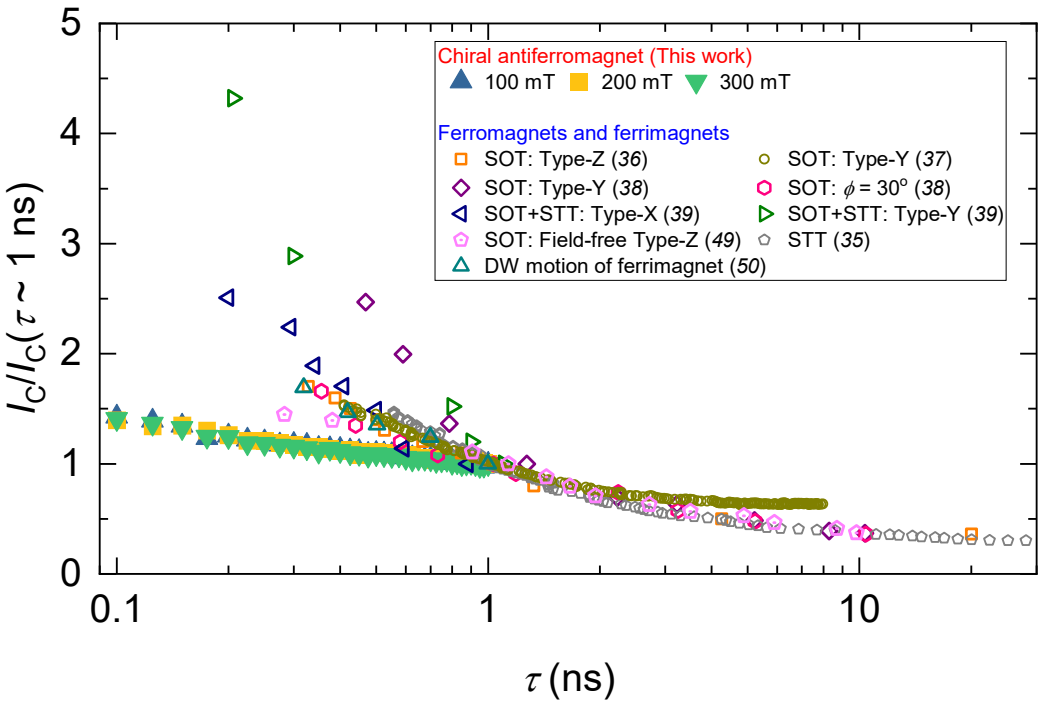

Fig. S9. Switching current versus pulse width. τ dependence of the I_C normalized by I_C at $\tau = 1$ ns in chiral antiferromagnetic Mn_3Sn nanodot and other nanoscale ferromagnetic and ferrimagnetic systems.

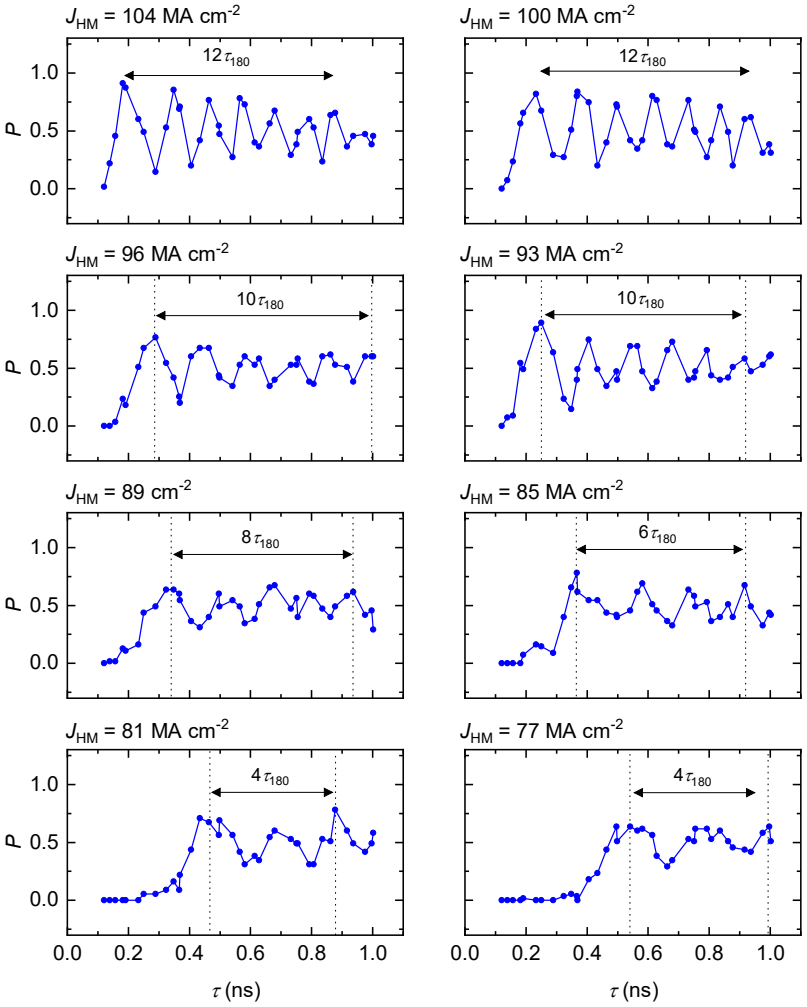

Fig. S10. Determination of the rotation frequency in chiral antiferromagnet from switching probability. τ dependence of P for various J_{HM}.

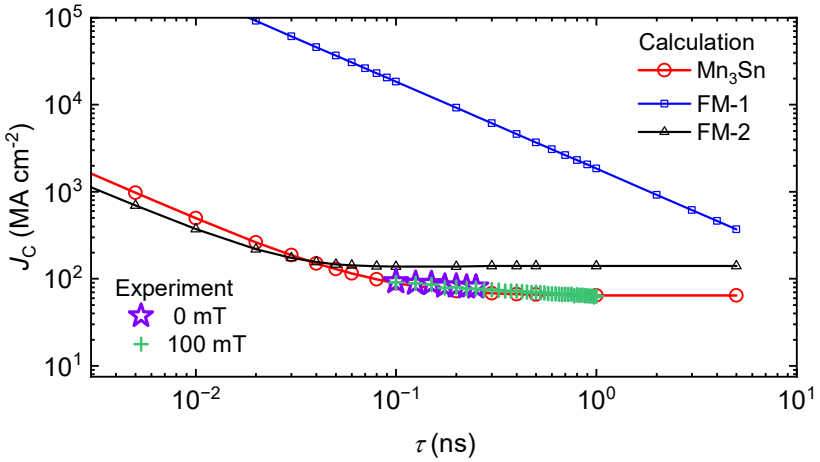

Fig. S11. Numerical calculation of switching current density: Comparison between chiral antiferromagnet and ferromagnet. Calculated J_C versus τ in Mn_3Sn, FM-1, and FM-2, and the experimental J_C in Mn_3Sn with different in-plane magnetic fields are shown by open symbols.

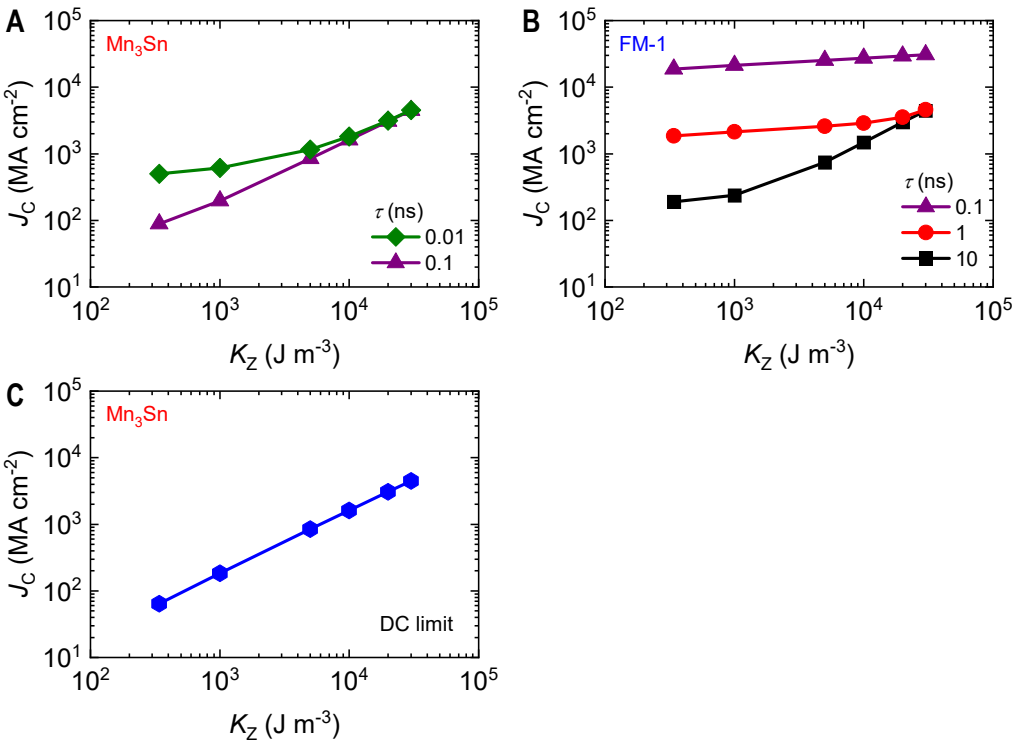

Fig. S12. Numerical calculation of switching current density: Dependencies on global magnetic anisotropy energy density. Calculated J_C versus K_Z for various τ in **(A)** Mn_3Sn and **(B)** FM-1. (C) The DC limit ($\tau \rightarrow \infty$) for Mn_3Sn.

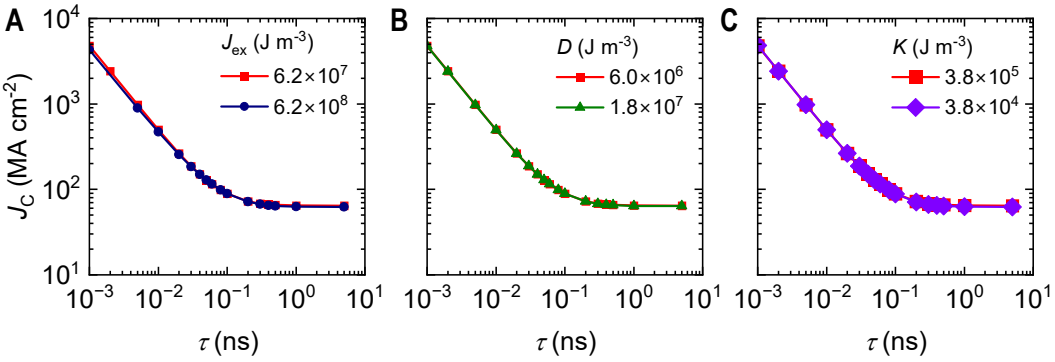

Fig. S13. Numerical calculation of switching current density: Dependencies on micromagnetic parameters. Calculated J_C versus τ, varying (A) the exchange coupling constant J_{ex}, (B) Dzyaloshinskii-Moriya coupling constant D, and (C) the local magnetic anisotropy K.

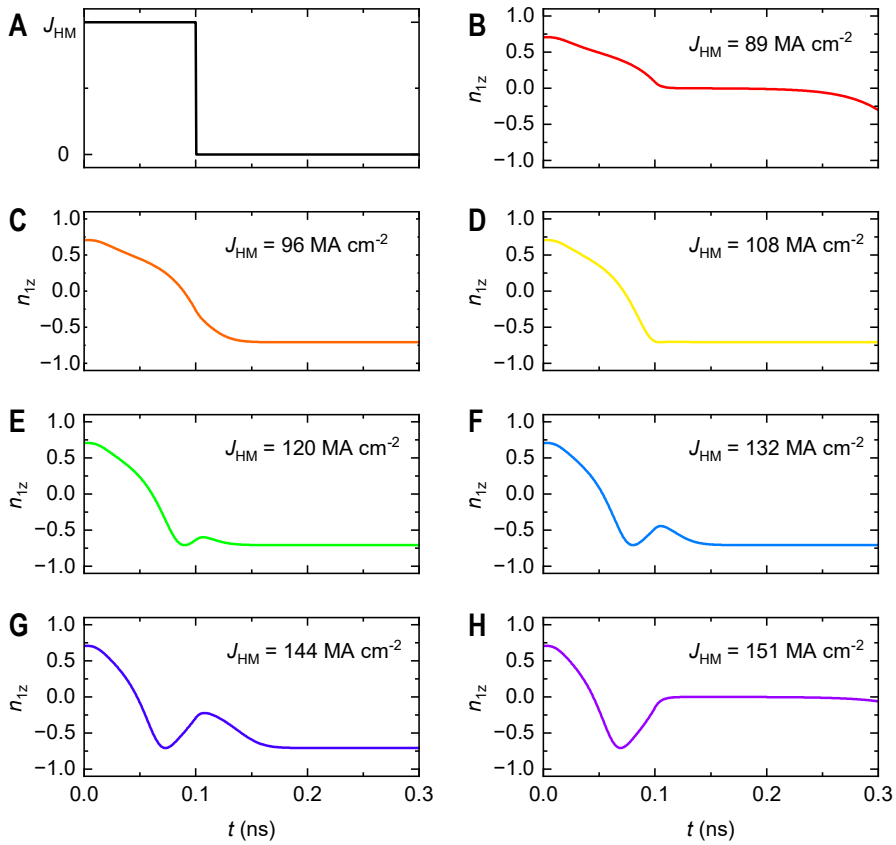

Fig. S14. Numerical calculation of antiferromagnetic order dynamics in time domain. (A) Current pulse shape employed in the simulation here, with the fixed width of 0.1 ns. (B)-(H) Calculated n_{1z} versus t, under various pulse amplitudes.